BRLR 1995

BRL

AD

ADA043845

(12)
NW

REPORT NO. 1995

SHAPED CHARGE JET PENETRATION
OF DISCONTINUOUS MEDIA

V. Kucher
J. Harrison

July 1977

D D C

RECEIVED

SEP 8 1977

B

Approved for public release; distribution unlimited.

AD No.
DDC FILE COPY

USA ARMAMENT RESEARCH AND DEVELOPMENT COMMAND
USA BALLISTIC RESEARCH LABORATORY
ABERDEEN PROVING GROUND, MARYLAND

REPORT DOCUMENTATION PAGE		READ INSTRUCTIONS BEFORE COMPLETING FORM
1. REPORT NUMBER BRL Report No. 1995	2. GOVT ACCESSION NO.	3. RECIPIENT'S CATALOG NUMBER
4. TITLE (and Subtitle) Shaped Charge Jet Penetration of Discontinuous Media.		5. TYPE OF REPORT & PERIOD COVERED Final rept. 6. PERFORMING ORG. REPORT NUMBER
7. AUTHOR(s) V. Kucher J. Harrison		8. CONTRACT OR GRANT NUMBER(s)
9. PERFORMING ORGANIZATION NAME AND ADDRESS US Army Ballistic Research Laboratory Aberdeen Proving Ground, Maryland 21005		10. PROGRAM ELEMENT, PROJECT, TASK AREA & WORK UNIT NUMBERS 1W161102AH43
11. CONTROLLING OFFICE NAME AND ADDRESS US Army Materiel Development & Readiness Command 5001 Eisenhower Avenue Alexandria, VA 22333		12. REPORT DATE JULY 1977 13. NUMBER OF PAGES 65 p.
14. MONITORING AGENCY NAME & ADDRESS(If different from Controlling Office)		15. SECURITY CLASS. (of this report) UNCLASSIFIED 15a. DECLASSIFICATION/DOWNGRADING SCHEDULE

16. DISTRIBUTION STATEMENT (of this Report)

Approved for public release; distribution nlimited.

DDC
RECEIVED
SEP 8 1977
RECEIVED
B

17. DISTRIBUTION STATEMENT (of the abstract entered in Block 20, if different from Report)

18. SUPPLEMENTARY NOTES

19. KEY WORDS (Continue on reverse side if necessary and identify by block number)

Penetration Mechanics
Hypervelocity Impact
Hydrodynamic Computer Code
Two-dimensional Computer Code

20. ABSTRACT (Continue on reverse side if necessary and identify by block number)

A computer study was made of the penetration by a copper rod, simulating a shaped-charge jet, into a steel plate backed-up by a semi-infinite medium. The parameters included impact velocity, steel plate thickness, and the material comprising the semi-infinite medium. The computer results were compared with a model of penetration based on Bernoulli's steady-state incompressible-flow equation.

DD FORM 1 JAN 73 1473 EDITION OF 1 NOV 65 IS OBSOLETE

UNCLASSIFIED
SECURITY CLASSIFICATION OF THIS PAGE (When Data Entered)

TABLE OF CONTENTS

LIST OF SYMBOLS

a   constant in Tillotson's equation of state

A   constant in Tillotson's equation of state

b   constant in Tillotson's equation of state

B   constant in Tillotson's equation of state

c   sound speed

c_o constant in sound speed equation

c_1 constant in sound speed equation

d_1^o penetration associated with t_1^o

d_1^f penetration associated with t_1^f

d_2^o penetration associated with t_2^o

G   modulus of rigidity

I   specific internal energy

I_M constant in yield strength equation

I_o constant in Tillotson's equation of state

I_s constant in Tillotson's equation of state

I_s' constant in Tillotson's equation of state

L   decrease in rod or jet length

$\left(\dfrac{L}{P}\right)_1$ steady-state ratio of rod loss to penetration in the plate

$\left(\dfrac{L}{P}\right)_2$ steady-state ratio of rod loss to penetration in the semi-infinite material

p   pressure

p_C pressure, condensed state

p_E pressure, expanded hot gases

P   depth of penetration or target thickness

r   radial coordinate

t_o time for rarefaction wave to travel the radius of the rod

$t_{1/2}$ time to penetrate 12.7 mm (½ in.) of plate material

t_1 time to penetrate 25.4 mm (1 in.) of plate material

t_1^o time at the beginning of V_1

t_2^o time at the beginning of V_2

t_1^f time at the end of V_1

V_o impact velocity

V_j jet velocity

V_p penetration velocity

V_1 steady-state velocity in the plate

V_2 steady-state velocity in the semi-infinite material

Y yield strength in shear

Y_o constant in yield strength equation

Y_1 constant in yield strength equation

Y_2 constant in yield strength equation

z longitudinal coordinate

α constant in Tillotson's equation of state

β constant in Tillotson's equation of state

Δr radial grid increment

Δz longitudinal grid increment

η $\dfrac{\rho}{\rho_o}$

μ $\eta - 1$

ν constant in the sound speed equation

ρ mass density

ρ_j mass density of the jet

ρ_o ambient mass density

ρ_t mass density of the target

6

I. INTRODUCTION

This report is concerned with the behavior of a shaped-charge jet when it penetrates a target possessing a material discontinuity, for example, a steel cover-plate on top of a thick aluminum plate. This study is limited to targets whose cover-plate material is more dense than the second material. A material discontinuity occurs at the interface between the two materials, and we shall refer to any interaction of the jet with this interface simply as rod-target interaction. A computer-oriented mathematical model was used in this study of rod-target interaction.

There are several two-dimensional models (codes) that were developed to handle penetration problems and are operational at the Ballistic Research Laboratory. These codes are OIL,[1] TOIL,[2] DORF,[3] and HELP,[4,5] which are Eulerian formulated, and HEMP,[6] which is Lagrangian formulated. The large deformation of material occurring during a shaped-charge penetration influenced the selection of one of the Eulerian codes for this study, and of these, the HELP code was selected because of its capability of denoting the material interfaces and free surfaces.

The objective of this computer study is to investigate the parameters affecting rod-target interaction in order to provide data on penetration and rod loss that could be used by armor experimentalists and designers. The results of the computer study, which are reported here, include only that part of the voluminous data generated by HELP that pertains to penetration depth and loss of rod material.

---

1. W. E. Johnson, "OIL, A Continuous Two-Dimensional Eulerian Hydrodynamic Code," Gulf General Atomic, GAMD-5580 Revised, January 1965.

2. W. E. Johnson, "TOIL, A Two-Material Version of the OIL Code," Gulf General Atomic, GAMD-8073 Addendum, November 1967.

3. Wallace E. Johnson, "Code Correlation Study," Air Force Weapons Laboratory Technical Report No. 70-144, April 1971.

4. L. J. Hageman and J. M. Walsh, "HELP, A Multi-Material Eulerian Program for Compressible Fluid and Elastic-Plastic Flows in Two Space Dimensions and Time, Volume I," Ballistic Research Laboratories Contract Report No. 39, May 1971. (AD #726459)

5. L. J. Hageman and J. M. Walsh, "HELP, A Multi-Material Eulerian Program for Compressible Fluid and Elastic-Plastic Flows in Two Space Dimensions and Time, Volume II: FORTRAN Listing of HELP," Ballistic Research Laboratories Contract Report No. 39, May 1971. (AD #726460)

6. Mark L. Wilkins, "Calculations of Elastic-Plastic Flow," University of California, Lawrence Radiation Laboratory, UCRL-7322, April 1963.

7

II. COMPUTER CODE

A. Description of the HELP Code

HELP (an acronym for Hydrodynamic ELastic Plastic) is a FORTRAN code developed by Systems, Science and Software, Inc. It evolved from three major hydrodynamic codes previously developed over a 20-year period. In chronological order of development, these codes are PIC,[7] OIL, and RPM.[8]

This code is Eulerian formulated, that is, a numerical mesh or grid is fixed in space and material is permitted to flow or move through the grid. Material motion is governed by the numerical approximations to the equations of conservation of mass, momentum, and energy. These equations along with an equation of state and a stress-strain relationship provide sufficient equations for their numerical solution.

HELP is time dependent in two space dimensions with an option for either plane (x,y) coordinates or cylindrical (r,z) coordinates. When the cylindrical coordinate option is used, the problems to be solved necessarily involve axisymmetric configurations such as spheres, cones, infinite plates, and right circular cylinders which impact normally upon axisymmetric targets. The time increment, which is determined by the code, is based on the Courant stability condition and the maximum sound speed plus the particle velocity in the grid.

The number of materials, which can be treated in one problem, is limited only by the size of the memory of the computer being used. The BRL version of HELP can handle three materials in addition to a vacuum. The different materials are separated from each other by lines joining massless tracer particles. These particles move across the grid and locate the interfaces and free surfaces of each material. Consequently, a Lagrangian effect is introduced into the treatment of moving surfaces.

The HELP code, using the von Mises yield condition, treats materials as being elastic-plastic.

The input for HELP involves the specification of initial density, specific internal energy, and velocity in each cell containing any material. Furthermore, locations of tracer particles along free surfaces and interfaces are specified.

---

7. Anthony A. Amaden, "The Particle-in-Cell Method for the Dynamics of Compressible Fluids," Los Alamos Scientific Laboratory of the University of California, LA-3466, February 1966.

8. J. K. Dienes, M. W. Evans, L. J. Hageman, W. C. Johnson, and J. M. Walsh, "An Eulerian Method for Calculating Strength Dependent Deformation. Part One, Part Two, Part Three, and Addendum," Gulf General Atomic, GAMD-8497, February 1968.

8

B. Computer Output

The output of the BRL version of HELP lists, at specified time intervals, the total internal energy, kinetic energy, mass, momentum components, and plastic work done for each material. The total energy, calculated for each computational cycle, must agree, within specified limits, with the total theoretical energy, otherwise, the computational process is brought to a halt.

The coordinates of the tracer particles are listed as well as, for each cell containing any material, the velocity components, hydrostatic pressure, specific internal energy, density, mass, and stress components.

Plotting programs have been developed at BRL to display the voluminous data generated during a typical computer run. Examples of the types of plots which can be generated are shown in Figures 1, 2, and 3. These plots were generated from data computed in this study; however, this type of information will not be reported here except for a brief description of these figures.

Figure 1 shows the pressure field at a particular time after the impact of a right circular rod on a plate backed by a semi-infinite material; Figure 2, the velocity field; and Figure 3, the stress field. In each of these figures the tracer particles were used to outline the interfaces and free surfaces of the different materials. Since the problem is axisymmetric, only half of the various fields are presented.

C. Equation of State

Since HELP has an equation-of-state subroutine, one may incorporate any equation of state into the program that is of the form where the pressure is a function of mass density and specific internal energy. The BRL version of HELP contains an equation of state for an ideal gas and also Tillotson's equation of state.[9]

Tillotson's equation of state takes two forms:
1. For the condensed states, that is, when $\rho > \rho_o$, or for any cold states, that is, when $I < I_s$,

$$p = p_C = \left[a + \frac{b}{\dfrac{I}{I_o \eta^2} + 1} \right] I\rho + A\mu + B\mu^2$$

2. For expanded hot gases, that is, when $\rho < \rho_o$ and $I > I_s$,

$$p = p_E = aI\rho + \left[\frac{bI\rho}{\dfrac{I}{I_o \eta^2} + 1} + A\mu e^{-\beta(1/\eta - 1)} \right] e^{-\alpha(1/\eta - 1)^2}$$

---

9. J. H. Tillotson, "Metallic Equations of State for Hypervelocity Impact," Gulf General Atomic, GA-3216, July 1962.

where

p = pressure
I = specific internal energy
ρ = mass density
$\eta = \rho/\rho_0$
$\mu = \eta - 1$

and a, b, A, B, α, β, ρ_0, I_0, I_s, and I'_s are constants for a particular material. The values of these constants for materials which were used in this report are listed in Table I.

In addition to Tillotson's equations, HELP provides a transition equation between the condensed and expanded states where $\rho < \rho_0$ and $I_s < I < I'_s$:

$$p = \frac{(I - I_s)\, P_E + (I'_s - I)\, P_C}{I'_s - I_s}.$$

Pressure versus particle-velocity Hugoniots and shock velocity versus particle velocity graphs, based on Tillotson's equations, are shown in Figures 4 and 5, respectively.

D. Strength

Several more material constants are required as inputs for HELP. The modulus of rigidity, G, relates the deviatoric stress to the deviatoric strain by a linear elastic relation. A variable yield strength in shear, defined by

$$Y = (Y_0 + Y_1\mu + Y_2\mu^2)\,(1 - I/I_M),$$

requires four additional constants. The values of these constants, for the materials used in this report, are given in Table II.[10]

III. ROD-TARGET PARAMETERS

The configuration of the jet and target for the computer study of rod-target interaction consisted of a copper rod, or jet, impacting normally upon a steel plate which, in turn, was backed-up by a semi-infinite material. The parameters for this study are listed in Table III.

The length of the rod was chosen to be long enough to prevent rod-end effects, such as shock reflections or rarefactions, from affecting the rod-target interaction. For simplicity, the rod, prior to impact, was given a uniform axial velocity; actually, a velocity gradient exists in a shaped charge jet.

---

10. *William Gillich and George E. Hauver, Inter-office correspondence, February 1970.*

10

It was not intended that all combinations of the parameters listed in Table III would be run on the computer; rather, the selection of combinations of parameters would be guided by the results of sets of computer runs. The runs were made at the Kirtland Air Force Base on the CDC 6600. The matrix of parameters for these runs is listed in Table IV in the order in which they were run.

IV. THEORY OF PENETRATION

Before presenting the numerical results obtained from the computer runs, we shall present some preliminary calculations of the penetration process for use as a comparison with the numerical results.

When a copper rod impacts upon a steel plate, shock waves immediately propagate from the interface into the steel plate and the copper rod. For a short time after impact, the high pressure in the region along and near the axis of symmetry of the rod-plate configuration and between the two diverging shocks remains constant. Eventually, rarefactions from the front surface of the plate and the sides of the rod will relieve this pressure. Estimates of the initial impact pressure and particle velocity can be obtained, by the method of reflected Hugoniots,[11] from Figure 4. Thereafter, Figure 5 can be used to determine the shock velocities. A summary of these values is presented in Table V.

The sound speed, c (km/s), in the high pressure region is determined from the relation[12]

$$c = c_o + c_1 p^\nu$$

where the constants c_o (km/s), c_1, and ν are 3.20, 3.405, and 0.452, respectively, for copper and 3.50, 3.259, and 0.439, respectively, for iron. The pressure, p, is in units of megabars.

An estimate of the time, t_o, required for the lateral rarefactions, coming from the edge of the contact surface, to reach the axis of symmetry of the rod-plate configuration is made by dividing the radius of the rod by the sound speed. Table VI sumarizes this information. Since the sound speed is greater in iron than copper, t_o was calculated from the sound speed of iron.

In the computer runs that were made, the 127-mm (5-in.) length of rod and the 12.7- mm (½-in.) and 25.4-mm (1-in.) plate thicknesses were large enough to prevent any disturbances, from the back of the plate or

11. R. Courant and K. O. Friedricks, *Supersonic Flow and Shock Waves*, *Volume I*, New York, Interscience Publishers, Inc., 1948.

12. Chester Grosch, "Sound Velocities Along the Hugoniot for Nine Metals at High Pressure," Stevens Institute of Technology, Unpublished note, January 1968.

11

the rear of the rod, from reducing the duration of constant pressure listed in Table VI.

Following the constant pressure phase of the penetration process, a steady-state phase begins. Here, the rate of penetration (the velocity of the rod-plate interface at the axis of symmetry) remains constant. This phase continues until disturbances from the interface of the plate and semi-infinite material interact with the main shock in the target.

A transient phase follows during which the rod-target interaction occurs. This phase is followed by another steady-state phase in which the penetration rate has adjusted itself to the semi-infinite material.

Estimates of the penetration velocity and the decrease in rod length during the steady-state phases can be made from the following relations based on Bernoulli's equation of incompressible flow:[13]

$$1. \quad V_p = \frac{V_j}{1 + (\rho_t/\rho_j)^{\frac{1}{2}}} \tag{1}$$

$$2. \quad P = L(\rho_j/\rho_t)^{\frac{1}{2}} \tag{2}$$

where

V_p = penetration velocity

V_j = jet velocity at impact

ρ_t = density of target

ρ_j = density of jet

P = depth of penetration or target thickness

L = decrease in jet length

Penetration velocities were calculated from Equation 1 for three jet velocities where the jet material was copper and the target material was varied. Assuming that the penetration velocity remains constant as the jet penetrates a steel target, the times, $t_{\frac{1}{2}}$ and t_1, required to penetrate 12.7 mm ($\frac{1}{2}$ in.) and 25.4 mm (1 in.) of steel, respectively, were also calculated. These data are listed in Table VII.

Figures 6, 7, and 8 show the displacement along the axis of symmetry, as a function of time, of the jet-target interface at impact velocities of 3, 5, and 7 km/s, respectively. Each target was a 25.4-mm (1-in.) plate of steel backed with various materials. These graphs were generated from the information in Table VII under the assumption that the rod was long enough to prevent end effects. Similar graphs could be plotted for a 12.7-mm ($\frac{1}{2}$-in.) plate.

---

13. E. M. Pugh, R. J. Eichelberger, and N. Rostoker, "Theory of Jet Formation with Lined Conical Cavities," Journal of Applied Physics, May 1952.

V. NUMERICAL RESULTS

Although a vast quantity of data is generated with each computer run of the HELP code, only data on the motion of the free surface and interfaces are reported here.

For every cycle of computation, the positions of three tracer particles were recorded. These tracer particles were located along the axis of symmetry at the base of the rod, the rod-plate interface, and the interface of the plate and semi-infinite material. Figure 9, which depicts the grid and projectile-target configuration used in these computer runs, shows the locations of these tracer particles.

With reference to the grid in Figure 9, the r-increment (the length of each cell in the r-direction), Δr, is equal to 0.0079375 mm for the first sixteen cells or columns; thereafter, the r-increment was increased geometrically, with a ratio of approximately 1.1, until a total of forty columns were dimensioned in the r-direction. The developer of HELP recommends that the geometric ratio does not exceed 1.5. The r-increment was increased in the r-direction to provide space for the shock waves, emanating from the impact region, to travel and be analyzed before reaching the right boundary of the fortieth column. This boundary is transmissive, that is, mass may flow through this boundary and out of the grid.

The grid consists of 90 cells or rows in the z-direction with the z-increment of the top 85 rows being equal to 0.018143 mm; thereafter, the z-increment, Δz, was increased geometrically over 14 rows in the negative z-direction with a ratio of approximately 1.1376. This increase in the z-increment provided space for the long rod. The bottom row had a Δz of 0.018143 mm; however, this dimension is not important since there was no material motion in this row. The top and the bottom of the grid were transmissive also.

The aspect ratio, $\Delta z / \Delta r$, was approximately 2.286 in the region where the r and z increments were constant. We would have preferred that the aspect ratio did not exceed 1.5, as recommended by the developer of HELP; however, the long, thin rod and the thickness of the target prohibited the use of a smaller aspect ratio. The radius of the rod was represented by only four cells which results in poor resolution of shock and rarefaction fronts. If a larger number of columns were used for the rod's radius, the Δr would have to be smaller and the aspect ratio would be increased.

With the constant Δz that was used, the thickness of the 25.4-mm (1-in.) plate was represented by 14 rows of cells and by 7 rows of cells for the 12.7-mm (½-in.) plate. Since a shock front is usually smeared over 4 or 5 cells, we should not expect good resolution of the shock front in the z-direction. The number of rows representing the plate could have been increased by increasing the number of rows in the grid; however, this would increase the running time and computer memory requirements for the the problem. With the grid that was used, the running time for each

13

case for approximately three hours with the use of 81,000 words of memory, which was near the capacity of the CDC 6600. Consequently, with the grid that was used, sharp shock detail was not expected; rather, a general picture of the penetration phenomena was expected.

The displacement, as a function of time, of the tracer particles, shown in Figure 9, were graphed in Figures 10-21 for the cases that were run on the computer. This information is not shown for Case 10 as there was difficulty in reading the data from the magnetic tape output of the computer. These graphs represent the prime output of the runs that were made. The following sections provide a discussion of these graphs and further information obtained from them.

VI. DISCUSSION

For all the cases that were run on the computer, the base of the rod moved at a constant velocity over the duration of the run as evidenced by the constant slope of the trajectory of the base tracer particle in Figures 10-21. This indicates that either none of the disturbances, initiated at the front end of the rod, reached the base of the rod during the time period considered or the code could not detect these disturbances.

The interface of the plate and the semi-infinite material begins to move before the rod-plate interface reaches it since a shock wave precedes the moving interface. Note that the thickness of the steel plate along the axis of symmetry decreases with time, but never becomes zero, that is, the plate is not perforated. This derives from the fact that, with the HELP code, a tracer particle, initially positioned on the axis of symmetry, cannot move off the axis, but only along the axis. Furthermore, these tracer particles cannot pass one another. Thus, some plate material will always separate the rod material from the semi-infinite material. In actuality, the plate would be perforated.

The displacement-time data from the computer output was interpolated to obtain $t_{\frac{1}{2}}$ and t_1, the time expended while the rod-plate interface tracer particle moved 12.7 mm ($\frac{1}{2}$ in.) and 25.4 mm (1 in.), respectively (depending on the thickness of the plate). See Table IX for a tabulation of these times. For a given velocity, these times increase as the density of the semi-infinite material is increased. A comparison of the data for an all steel target (where the semi-infinite material is steel) with the data in Table VII indicates that $t_{\frac{1}{2}}$ and t_1, obtained from Bernoulli's incompressible equation, are less than that obtained from the compressible material code, HELP.

If we measure penetration from the initial position of the free surface of the steel plate, the displacement of the rod-plate tracer particle gives us penetration. Penetration trajectories are shown in Figures 22 and 23 for plate thicknesses of 12.7 mm ($\frac{1}{2}$ in.) and 25.4 mm (1 in.), respectively. One may wish to compare Figure 23 with Figures 6,

14

7, and 8 to see the difference between the compressible and incompressible mathematical models of penetration.

Examining Figure 23, we see that the penetration process starts with a fluctuation, the duration of which appears to decrease as the impact velocity is increased. The duration of this period is denoted by t_1^o. A steady-state period, characterized by a constant slope (velocity), of the penetration trajectories, follows and lasts until a time denoted by t_1^f.

Following t_1^f, the penetration trajectories pass through a transition period ending at time t_2^o, which marks the beginning of another steady-state period. Rod-target interaction occurs between t_1^f and t_2^o; this will be discussed later.

To gain further information on the penetration process, let us examine the penetration velocity histories of the cases which were run on the computer. The penetration velocity - time curves, shown in Figures 24 and 25, were obtained by fitting cubic spline functions[14] to the data in Figures 22 and 23 and taking the first derivatives of the functions. Using the data in Figures 22 and 23, we have also plotted penetration velocity - penetration curves as shown in Figures 26 and 27. These velocity curves show that the penetration process starts out with a fluctuation in velocity, as pointed out previously.

The steady-state velocity, V_1, between t_1^o and t_1^f, was determined by a least-squares fit to the data that was close to being a straight line. This velocity is listed in Table IX. The steady-state velocity, V_2, which occurs after t_2^o, was similarly determined and is also listed in Table IX. The values for V_1 and V_2 tend to average about 6% less than the values listed for V_p in Table VII.

The values of the times, t_1^o, t_2^o, and t_1^f, which are tabulated in Table IX, were determined by estimating when V_1 and V_2 began and when V_1 ended. If we compare t_o in Table VI with t_1^o in Table IX, we find that it takes an order of magnitude more time to reach a steady-state velocity than for a rarefaction wave to reach the axis of symmetry of the rod-target configuration.

---

14. Palmer R. Schlegel, "Approximate by Cubic Spline with Respect to Euclidean Norm," Ballistic Research Laboratories Report No. 1465, January 1970. (AD #700973)

15

Figures 22 and 23 were used to determine d_1^o, d_1^f, and d_2^o, the penetration distances corresponding to times, t_1^o, t_1^f, and t_2^o, respectively. These distances are listed in Table IX.

The rod loss, L, was determined by subtracting the distance between the base tracer particle and the rod-plate interface tracer particle (Figures 10-22) from the initial length of the rod, 127 mm (5 in.). This information is presented as rod loss - penetration curves in Figures 28-31. By a least-squares fit of the data in these figures that were close to a straight line, we determined the rod loss to penetration ratios for the plate material and the semi-infinite material, $\left(\frac{L}{P}\right)_1$ and $\left(\frac{L}{P}\right)_2$, respectively. These ratios, which are listed in Table IX, are greater than the values of $\frac{L}{P}$ in Table VIII for incompressible flow.

Between the penetration distances of d_1^f and d_2^o, the slope of the curves in Figures 28-31 is changing. This is the transition region where the penetration process is affected by the unlike material interface in the target. Between d_1^f and a penetration distance equal to the original thickness of the plate, the gradient of the rod loss, with respect to penetration, starts to decrease. Guided by Equation 2, we could say that the plate material was acting as if it were less dense than normal. After a penetration distance greater than the original plate thickness, and less than d_2^o, is reached, the rod-loss gradient, with respect to penetration, is greater than that finally obtained in the steady-state region in the semi-infinite material. Again according to Equation 2, we could say that the semi-infinite material was acting as if it were more dense than normal.

From Figures 10-22, we observe that, not only is the thickness of the steel plate (the distance between the rod-plate tracer particle and the tracer particle for the interface of the plate and the semi-infinite material) decreasing along the axis of symmetry, but, more important, some of the plate material has been pushed into the region initially occupied by the semi-infinite material. For example, Figure 10 indicates that approximately 4.06 mm (0.16 in.) of plate material has moved into this region when the rod has penetrated a distance of 25.4 mm (1 in.), the original thickness of the plate. This is one of the reasons that the semi-infinite material is acting as if it were more dense than normal.

A method that we could use to gauge the relative merits of various materials in hindering penetration is by using Equation 2 to determine an apparent target density. The density of the rod would be the initial copper density and the ratio, $\frac{L}{P}$, would be determined from the numerical

16

results. However, since the penetration velocity histories have already
been determined, Equation 1 will be used for this purpose. This
analysis is shown in Figures 32-35, where the apparent density has been
normalized with respect to the initial density of steel for the first
25.4 mm (1 in.) (the initial thickness of the plate) of penetration;
thereafter, the target density, obtained from Equation 1, has been
normalized with respect to the initial density of the semi-infinite
material. Of course, this normalization is undefined for a vacuum.

Examining Figure 33, we again see fluctuations in the curves during
the initial penetration process. Next comes the steady-state region
where, as we previously pointed out, the penetration velocity obtained
from the numerical results was less than that determined from the
incompressible flow theory. This difference in velocity accounts for
the normalized density being greater than unity as one would expect.
Nevertheless, some information on the effect of the material of the
semi-infinite medium on rod loss can be obtained from this analysis
when we look ·: .h: transition region between the two steady-state
regions.

Just , .f.:re 25.4 mm (1 in.) of penetration, we see that the
semi-infinite material with the lower initial density (aluminum compared
to titanium) provides a lower apparent density for the steel plate.
Thus, the less dense semi-infinite medium causes less rod loss in this
region than a more dense medium. However, just after 25.4 mm (1 in.) of
penetration, the semi-infinite material with the lower initial density
(aluminum compared to titanium) provides a higher apparent density for
the semi-infinite medium. Thus, the less dense semi-infinite medium
causes more rod loss in this region compared to a more dense medium.

An apparent density curve for air as a semi-infinite material was
not plotted since its low density, compared to the density of the metals
that were used as semi-infinite material, resulted in apparent densities
that were three orders of magnitude greater than shown in Figures 32-35.

A comparison of the steel-aluminum curves in Figures 32-34 does
not indicate any clear effect of impact velocity on the apparent density
of the semi-infinite material.

VII. SUMMARY

The results from a set of computer runs, designed to investigate
the interaction of a copper rod, simulating a shaped-charge jet, with
the interface of the target materials, were presented. The results were
mainly concerned with the penetration process as viewed along the axis
of symmetry of the rod-target configuration.

A comparison of the numerical (unsteady, compressible) results with
the results from Bernoulli's incompressible equations shows that the
latter results may be satisfactory for predicting rod loss, penetration
velocity, etc. for many purposes; however, for an experimentalist or

17

armor designer to take full advantage of phenomena which can hinder penetration, compressibility should be taken into account.

The numerical results show that the penetration process starts with a fluctuation in the penetration velocity, followed by a steady-state period. Naturally, this steady-state period will occur only if the target plate is thick enough. The results fr m the runs of the 12.7-mm (½-in.) plate indicate that this thickness was just about on the borderline for not getting a steady-state condition. Following the steady-state period, a transition period occurs as the penetration velocity adjusts to the final steady-state velocity.

This transition region can be divided into two zones: one before a penetration distance, equal to the initial thickness of the plate, is reached and one after this depth is reached.

In the first zone, the apparent density of the steel is lower than its normal density, thus, the rate of rod loss is reduced and the penetration process is assisted. In the second zone, the apparent density of the semi-infinite material is greater than its normal density, thus, increasing the rate of rod loss over that which is normally expected for a given material. One reason for this increase in apparent density is that some of the steel plate was pushed into the region which was initially occupied by the semi-infinite material.

The thickness of material in the second zone, necessary for rod-target interaction to be completed, depends on the density of the semi-infinite material and the impact velocity. For an impact velocity of 7 km/s, rod-target interaction ceases after a penetration of about 30.5 mm (1.2 in.) into a vacuum, 21.6 mm (0.85 in.) into air, and 17.5 mm (0.69 in.) into aluminum. However, for an impact velocity of 3 km/s, rod-target interaction ceases after about 5.1 mm (0.20 in.) of penetration into aluminum.

REFERENCES

1. W. E. Johnson, "OIL, A Continuous Two-Dimensional Eulerian Hydrodynamic Code," Gulf General Atomic, GAMD-5580 Revised, January 1965.

2. W. E. Johnson, "TOIL, A Two-Material Version of the OIL Code," Gulf General Atomic, GAMD-8073 Addendum, November 1967.

3. Wallace E. Johnson, "Code Correlation Study," Air Force Weapons Laboratory Technical Report No. 70-144, April 1971.

4. L. J. Hageman and J. M. Walsh, "HELP, A Multi-Material Eulerian Program for Compressible Fluid and Elastic-Plastic Flows in Two Space Dimensions and Time, Volume I," Ballistic Research Laboratories Contract Report No. 39, May 1971. (AD #726459)

5. L. J. Hageman and J. M. Walsh, "HELP, A Multi-Material Eulerian Program for Compressible Fluid and Elastic-Plastic Flows in Two Space Dimensions and Time, Volume II: FORTRAN Listing of HELP," Ballistic Research Laboratories Contract Report No. 39, May 1971. (AD #726460)

6. Mark L. Wilkins, "Calculations of Elastic-Plastic Flow," University of California, Lawrence Radiation Laboratory, UCRL-7322, April 1963.

7. Anthony A. Amaden, "The Particle-in-Cell Method for the Dynamics of Compressible Fluids," Los Alamos Scientific Laboratory of the University of California, LA-3466, February 1966.

8. J. K. Dienes, M. W. Evans, L. J. Hageman, W. E. Johnson, and J. M. Walsh, "An Eulerian Method for Calculating Strength Dependent Deformation. Part One, Part Two, Part Three, and Addendum," Gulf General Atomic, GAMD-8497, February 1968.

9. J. H. Tillotson, "Metallic Equations of State for Hypervelocity Impact," Gulf General Atomic, GA-3216, July 1962.

10. William Gillich and George E. Hauver, Inter-office correspondence, February 1970.

11. R. Courant and K. O. Friedricks, Supersonic Flow and Shock Waves, Volume I, New York, Interscience Publishers, Inc., 1948.

12. Chester Grosch, "Sound Velocities Along the Hugoniot for Nine Metals at High Pressure," Stevens Institute of Technology, Unpublished note, January 1968.

13. E. M. Pugh, R. J. Eichelberger, and N. Rostoker, "Theory of Jet Formation with Lined Conical Cavities," Journal of Applied Physics, May 1952.

14. Palmer R. Schlegel, "Approximate by Cubic Spline with Respect to Euclidean Norm," Ballistic Research Laboratories Report No. 1465, January 1970. (AD #700973)

TABLE I

CONSTANTS FOR TILLOTSON'S EQUATION OF STATE[5]

Material	a	b	A	B	I_o	ρ_o	α	β	I_s	I'_s
			dynes/cm^2	dynes/cm^2	ergs/gm	gm/cm^3			ergs/gm	ergs/gm
Al	.5	1.63	0.75×10^{12}	0.65×10^{12}	0.50×10^{11}	2.79	5	5	3.00×10^{10}	15.0×10^{10}
Cu	.5	1.5	1.39×10^{12}	1.10×10^{12}	3.25×10^{11}	8.9	5	5	1.38×10^{10}	6.9×10^{10}
Fe	.5	1.5	1.28×10^{11}	1.05×10^{12}	0.95×10^{11}	7.8	5	5	2.44×10^{10}	10.2×10^{10}
Ti	.5	0.60	1.03×10^{12}	0.50×10^{12}	0.70×10^{11}	4.5	5	5	3.50×10^{10}	12.5×10^{10}

Note: The units are reported as used in the HELP code.

TABLE II

MATERIAL CONSTANTS

Material	G $dyne/cm^2$	Y_o $dyne/cm^2$	Y_1	Y_2	I_M ergs/gm
7075-T6 Al	2.7×10^{11}	2.9×10^9	0	0	0.85×10^{10}
Cu	4.57×10^{11}	1.275×10^9	0	0	0.67×10^{10}
8630 Steel	7.86×10^{11}	6.8×10^9	0	0	1.32×10^{10}
Ti	3.755×10^{11}	2.586×10^9	0	0	1.556×10^{10}

Note: The units are reported as used in the HELP code.

21

TABLE III

ROD-TARGET PARAMETERS

Rod diameter   0.25 in. (6.35 mm)

Rod length   5.0 in. (127.0 mm)

Rod density   8.9 Mg/m^3 (copper)

Rod impact velocity   3, 5, and 7 km/s

Plate density   7.8 Mg/m^3 (steel)

Plate material   Armor steel and mild steel

Plate thickness   0.5 in. (12.7 mm) and 1.0 in. (25.4 mm)

Density of semi-infinite material   0.0 (vacuum), 1.2929×10^{-3} (air),
2.79 (aluminum), 4.5 (titanium),
and 7.8 (steel) Mg/m^3

TABLE IV

COMPUTATIONAL MATRIX

Rod diameter   0.25 in. (6.35 mm)

Rod length   5.0 in. (127 mm)

Rod density   8.9 Mg/m^3 (copper)

Plate density   7.8 Mg/m^3 (steel)

Plate material 8630 armor steel

Case	Impact Velocity	Plate Thickness		Semi-infinite Material
	km/s	in.	mm	
3	7	1.0	25.4	7075-T6 Al
5	7	1.0	25.4	Air
6	7	1.0	25.4	Vacuum
7	7	1.0	25.4	8360 steel
9	3	1.0	25.4	8360 steel
10	3	1.0	25.4	Ti
11	3	1.0	25.4	7075-T6 Al
12	7	0.5	12.7	Ti
13	7	0.5	12.7	7075-T6 Al
14	7	0.5	12.7	8630 steel
15	5	1.0	25.4	8630 steel
16	5	1.0	25.4	Ti
17	5	1.0	25.4	7075-T6 Al

23

TABLE V

SHOCK PROPERTIES FOR COPPER ROD - STEEL PLATE IMPACT

Impact Velocity km/s	Impact Pressure Mbar	Particle Velocity km/s	Shock Velocity km/s	
			Copper	Steel
3	0.8	1.57	6.26	6.34
5	1.7	2.71	8.02	8.00
7	2.7	3.67	9.45	9.30

TABLE VI

SOUND SPEED AND DURATION OF CONSTANT PRESSURE

Impact Pressure Mbar	Sound Speed km/s		t_o μs
	Copper	Iron	
0.8	6.28	6.45	0.492
1.7	7.53	7.61	0.417
2.7	8.53	8.54	0.372

TABLE VII

PENETRATION VELOCITY

V_j km/s	Material	V_p km/s	$t_{\frac{1}{2}}$ μs	t_1 μs
3	Vacuum	3.000		
3	Air	2.964		
3	Al	1.923		
3	Ti	1.753		
3	Steel	1.549	8.199	16.398
5	Vacuum	5.000		
5	Air	4.940		
5	Al	3.205		
5	Ti	2.922		
5	Steel	2.582	4.919	9.837
7	Vacuum	7.000		
7	Air	6.917		
7	Al	4.487		
7	Ti	4.091		
7	Steel	3.615	3.513	7.026

TABLE VIII

ROD LOSS

Material	L/P
Vacuum	0.0
Air	0.0121
Al	0.5599
Ti	0.7111
Steel	0.9361

TABLE IX

PENETRATION DATA

Case	Semi-Infinite Material	Impact Velocity km/s	Plate Thickness in.	t_3 us	t_1 us	v_1 km/s	t_1^o us	d_1^o in.	t_1^f us	d_1^f in.	v_2 km/s	t_2^o us	d_2^o in.	$(\frac{L}{F})_1$	$(\frac{L}{F})_2$
11	Al	3	1	-	17.442	1.39	2.77	0.164	12.0	0.679	1.7	20.5	1.20	1.17	0.74
9	Steel	3	1	-	17.923	1.39	2.77	0.164	-	-	-	-	-	1.17	-
17	Al	5	3	-	10.136	2.43	1.98	0.198	5.73	0.557	3.2	17.5	1.85	1.06	0.59
16	Ti	5	1	-	10.231	2.42	3.22	0.317	6.15	0.596	2.8	16.0	1.62	1.06	0.73
15	Steel	5	1	-	10.373	2.42	3.11	0.307	-	-	-	-	-	1.06	-
6	Vacuum	7	1	-	7.083	3.38	2.29	0.333	4.81	0.672	*	13.0	2.20	1.07	0.13
5	Air	7	1	-	7.065	3.38	2.29	0.333	4.76	0.661	*	11.9	1.85	1.07	0.14
3	Al	7	1	-	7.188	3.38	2.23	0.325	5.06	0.703	4.3	11.5	1.69	1.07	0.63
7	Steel	7	1	-	7.275	3.38	2.43	0.394	-	-	-	-	-	1.07	-
13	Al	7	3	3.458	-	3.46	2.08	0.304	2.40	0.347	4.3	7.0	1.07	1.07	0.65
12	Ti	7	3	3.487	-	3.43	2.21	0.322	2.51	0.361	3.8	*	*	1.07	*
14	Steel	7	3	3.547	-	3.43	1.79	0.264	-	-	-	-	-	1.07	-

Key: -, not applicable
*, information could not be determined

26
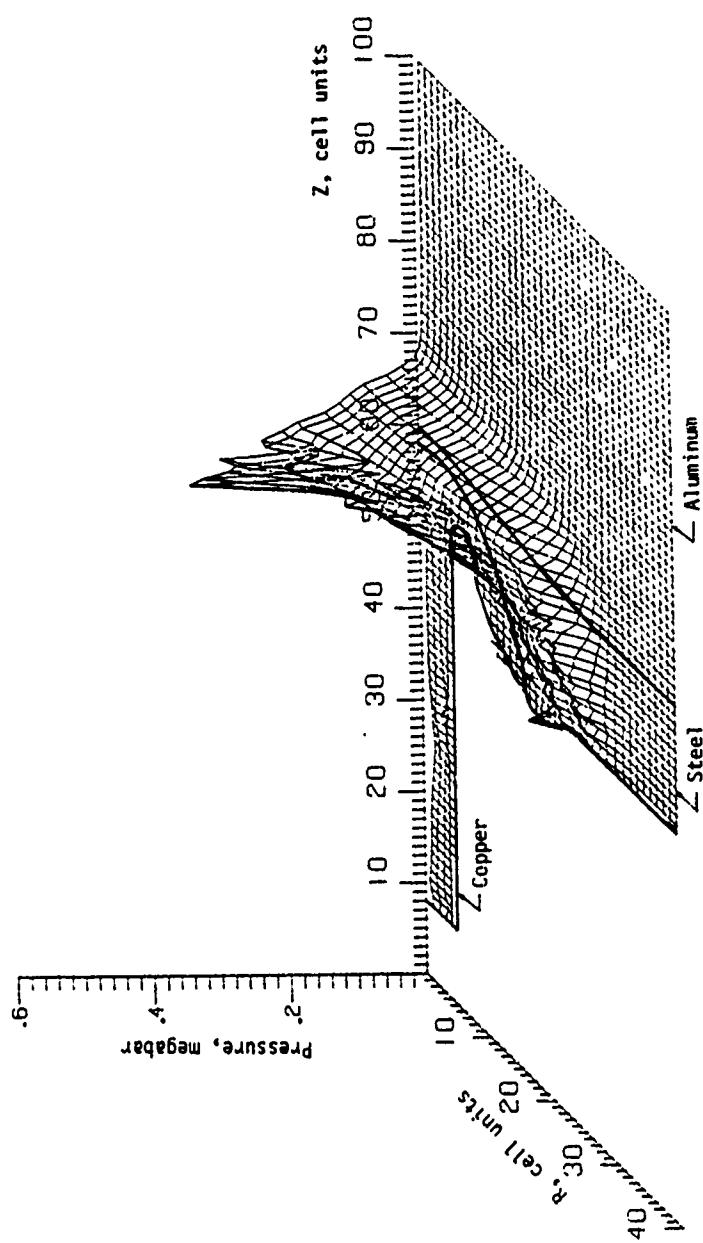
Figure 1 (U). The hydrostatic pressure field, at 7.345 μsec (computational cycle #300) after the impact of a copper rod on a laminate target, is shown with an outline of the rod-target configuration.
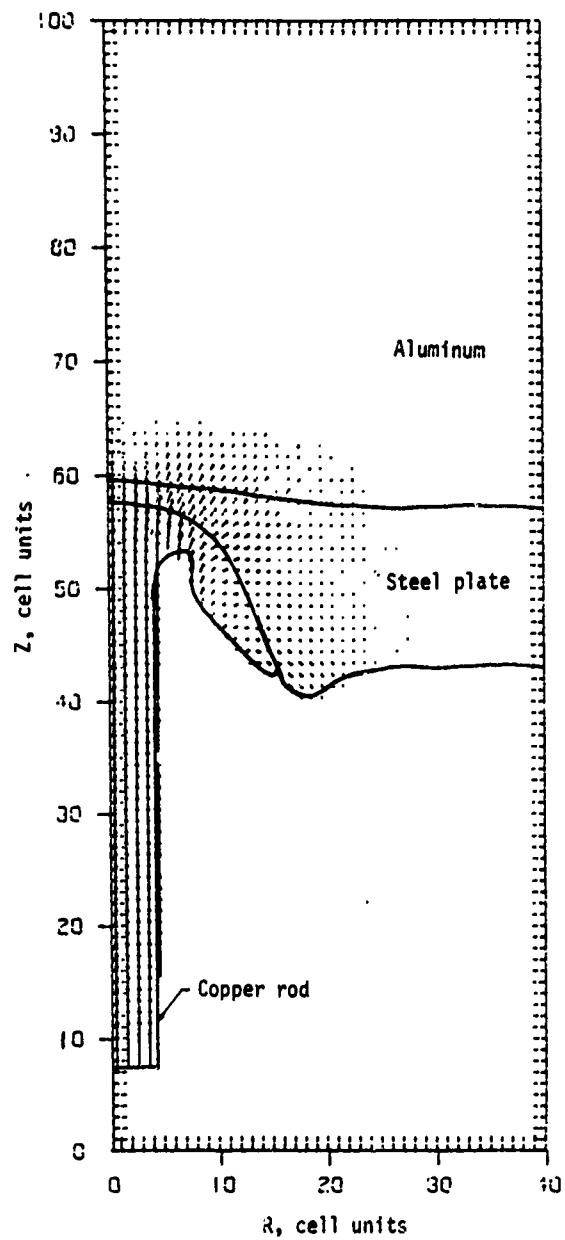
Figure 2 (U). The velocity field, at 7.345 usec (computational cycle #300) after the impact of a copper rod on a laminate target, is shown with an outline of the rod-target configuration.

28

PRINCIPAL DIVIATORIC STRESS FIELD
10 UNITS=0.1 MBAR

PRINCIPAL TOTAL STRESS FIELD
10 UNITS=1.0 MBAR
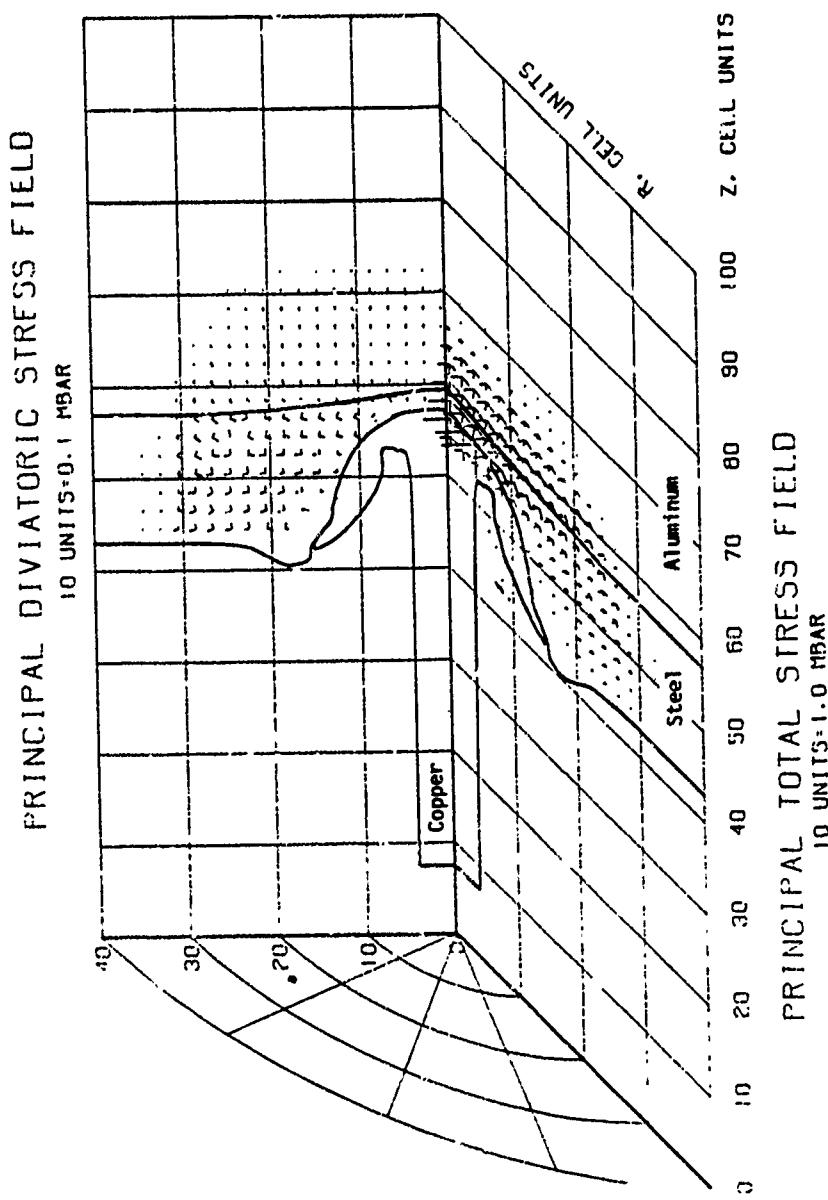
Figure 3 (U). The principal deviatoric and total stress fields, at 7.345 µsec (computational cycle #300) after the impact of a copper rod on a laminate target, are shown with an outline of the rod-target configuration.

29

PARTICLE VELOCITY, CM/MICROSEC
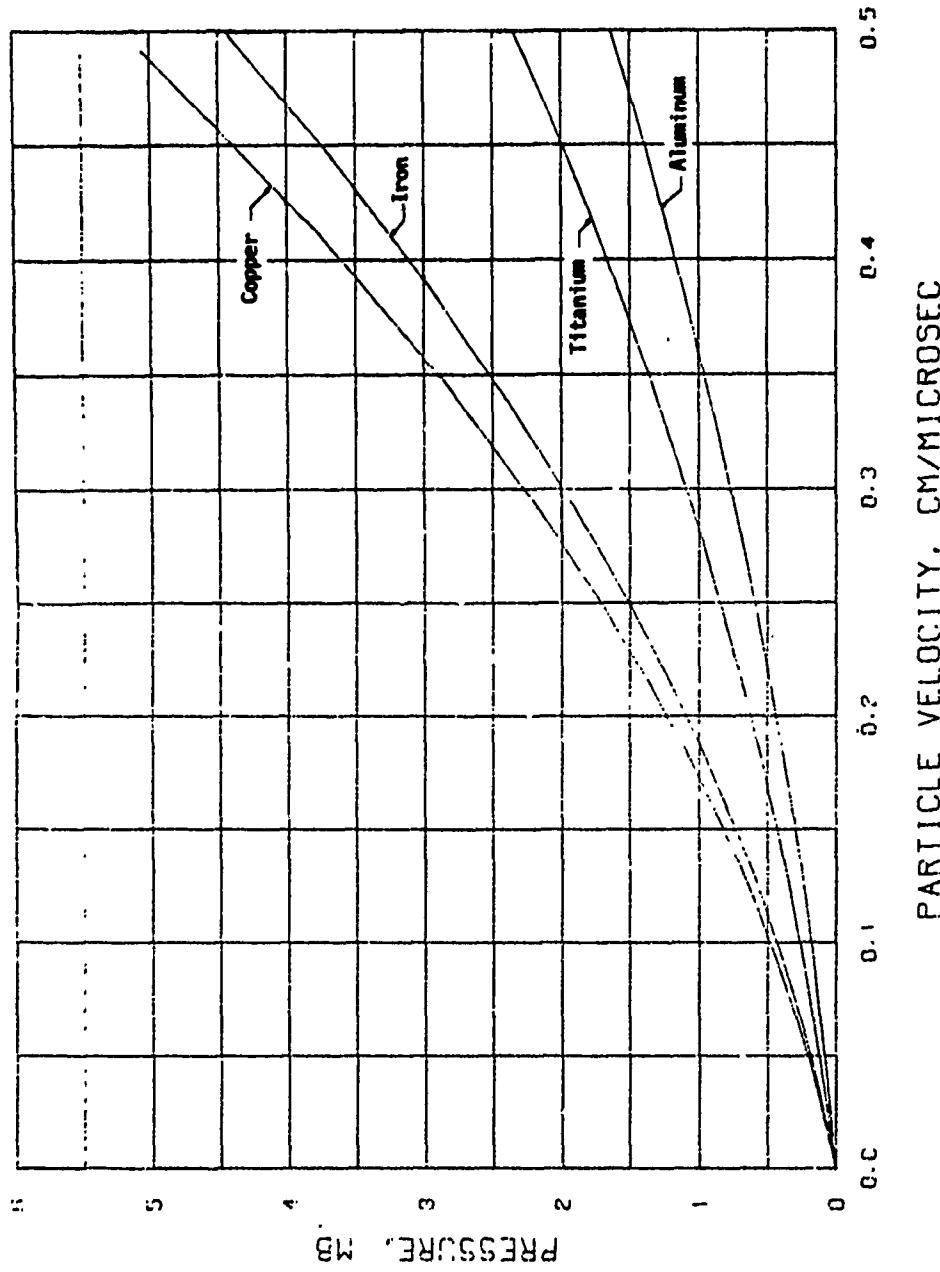
Figure 4 (U). Hugoniot Curves Based on Tillotson's Equation of State

30
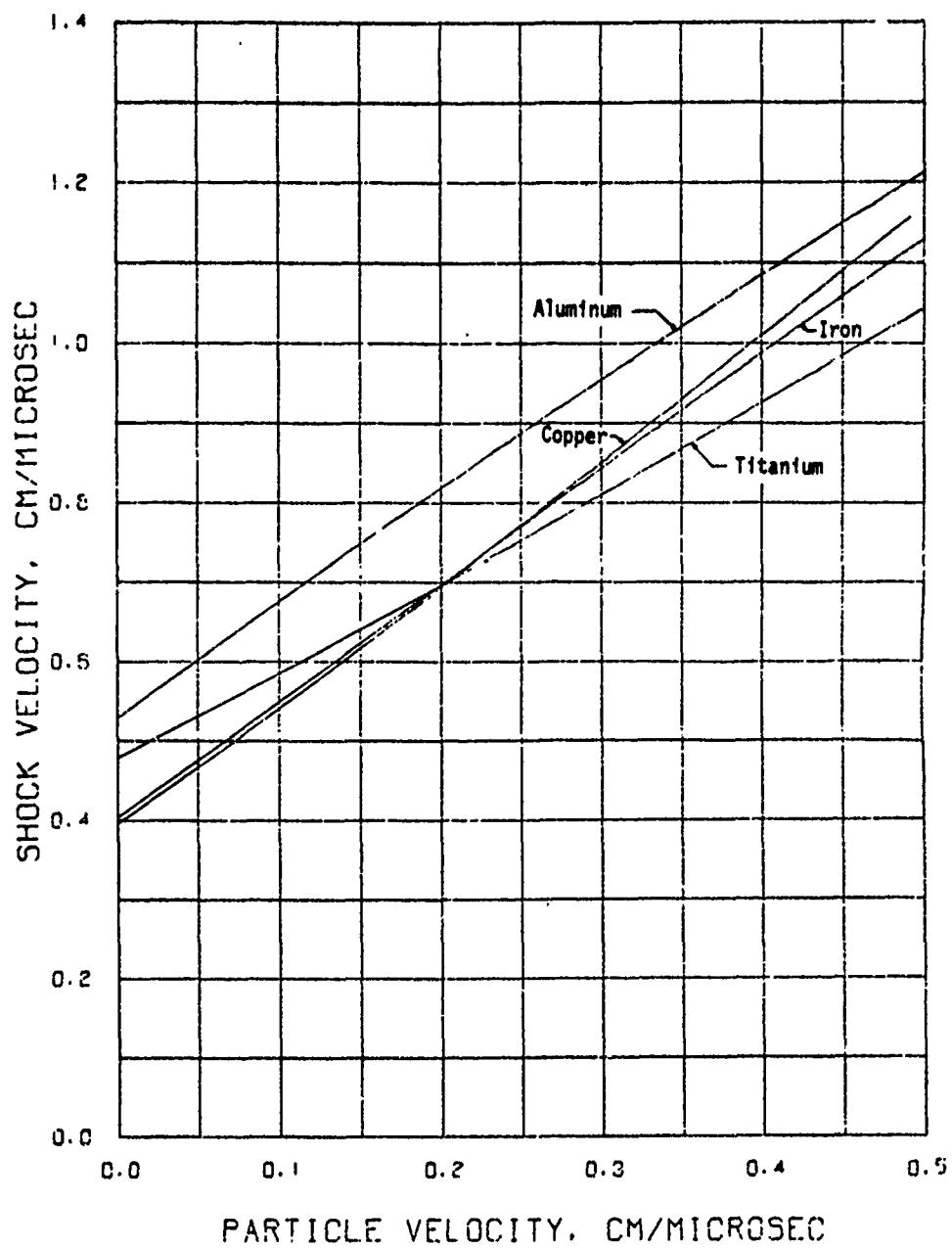
Figure 5 (U). Shock Velocity - Particle Velocity Curves for Various Materials

31

TIME. MICROSEC
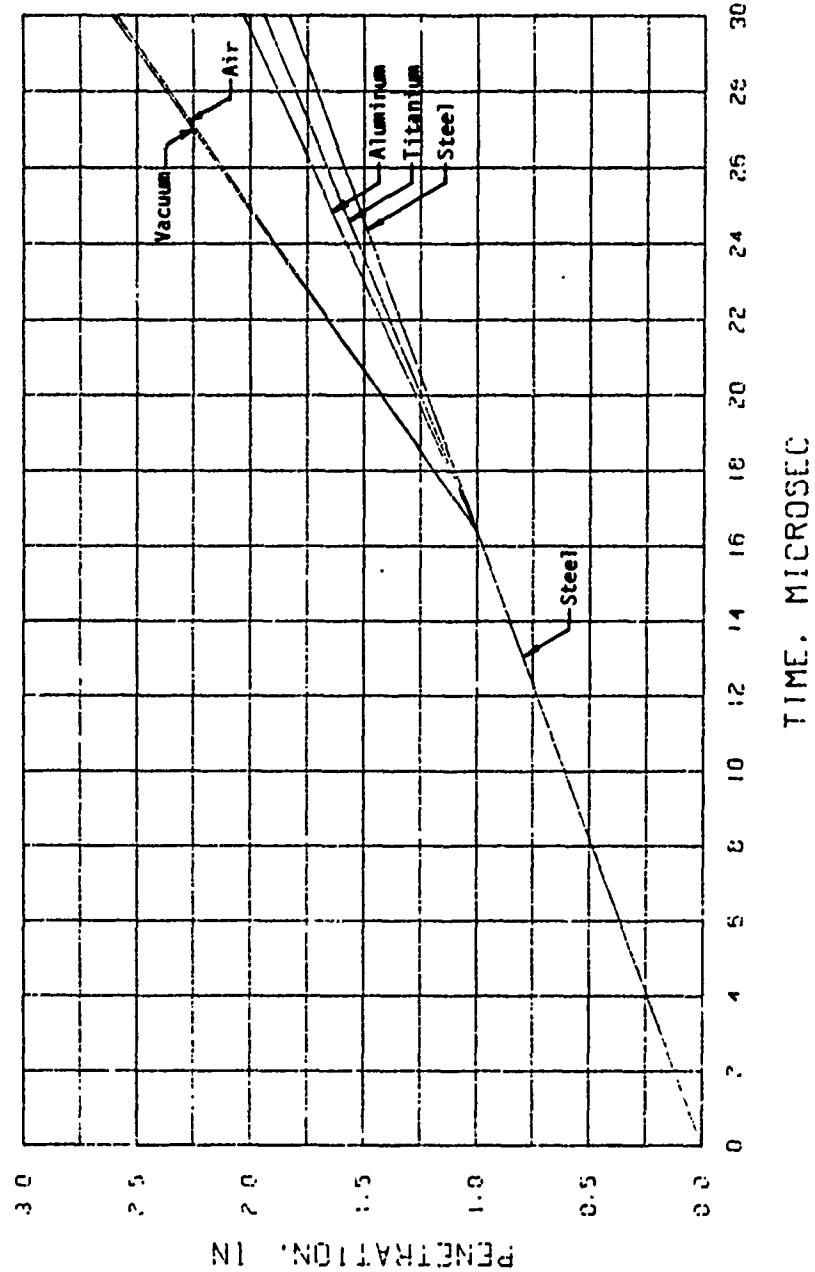
Figure 6 (U). The effect of various materials, backing a 1-in. steel plate, on the penetration history of a copper rod impacting at V_0 = 3 mm/μsec is shown. These curves are based on an incompressible hydrodynamic model.

32

TIME. MICROSEC
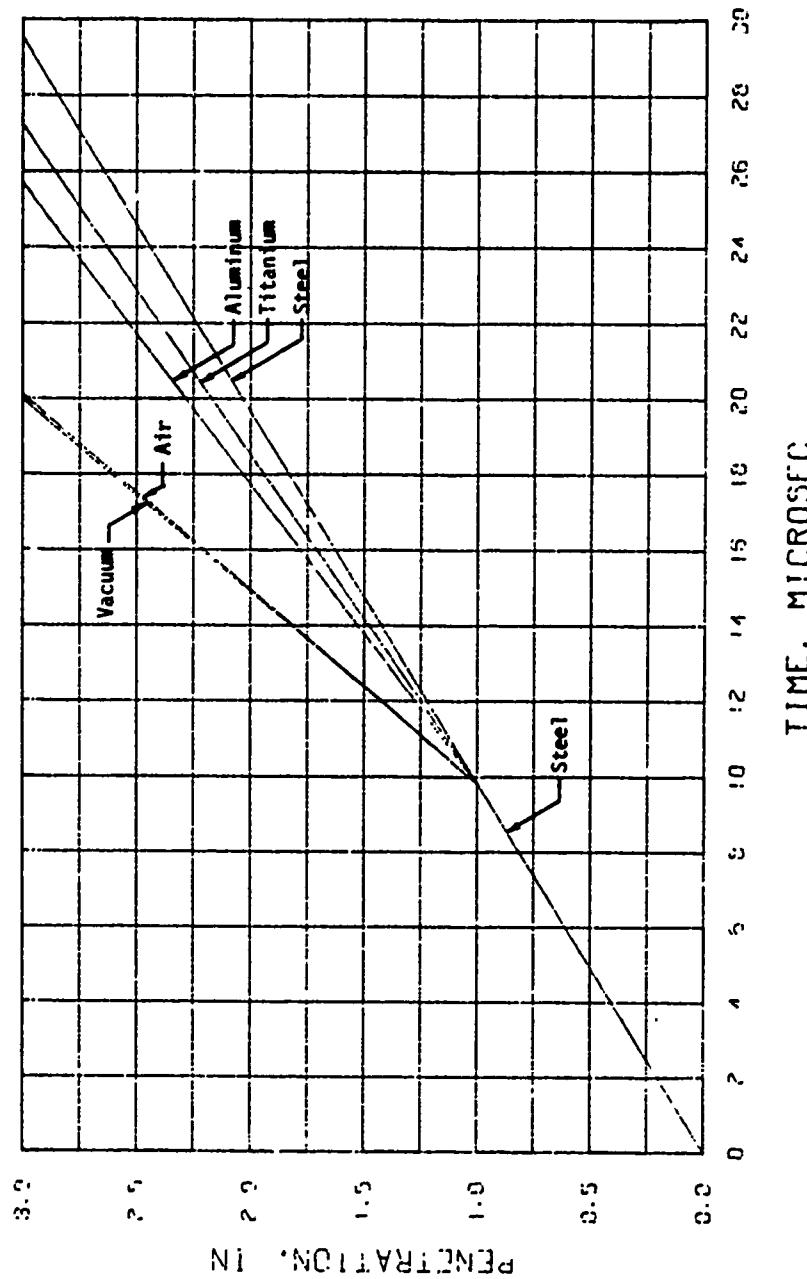
Figure 7 (U). The effect of various materials, backing a 1-in. steel plate, on the penetration history of a copper rod impacting at V_0 = 5 mm/μsec is shown. These curves are based on an incompressible hydrodynamic model.

33

TIME, MICROSEC
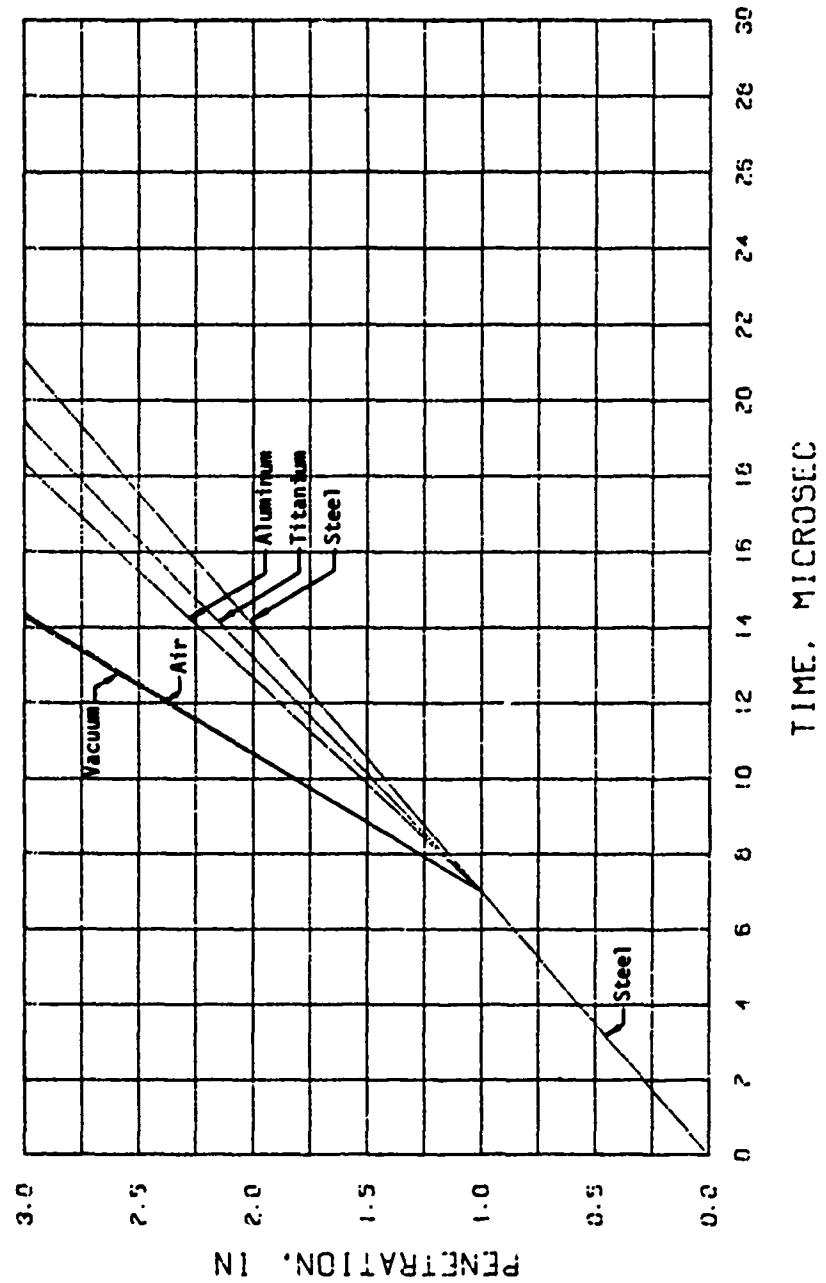
Figure 8 (U). The effect of various materials, backing a 1-in. steel plate, on the penetration history of a copper rod impacting at $V_o = 7$ mm/μsec is shown. These curves are based on an incompressible hydrodynamic model.
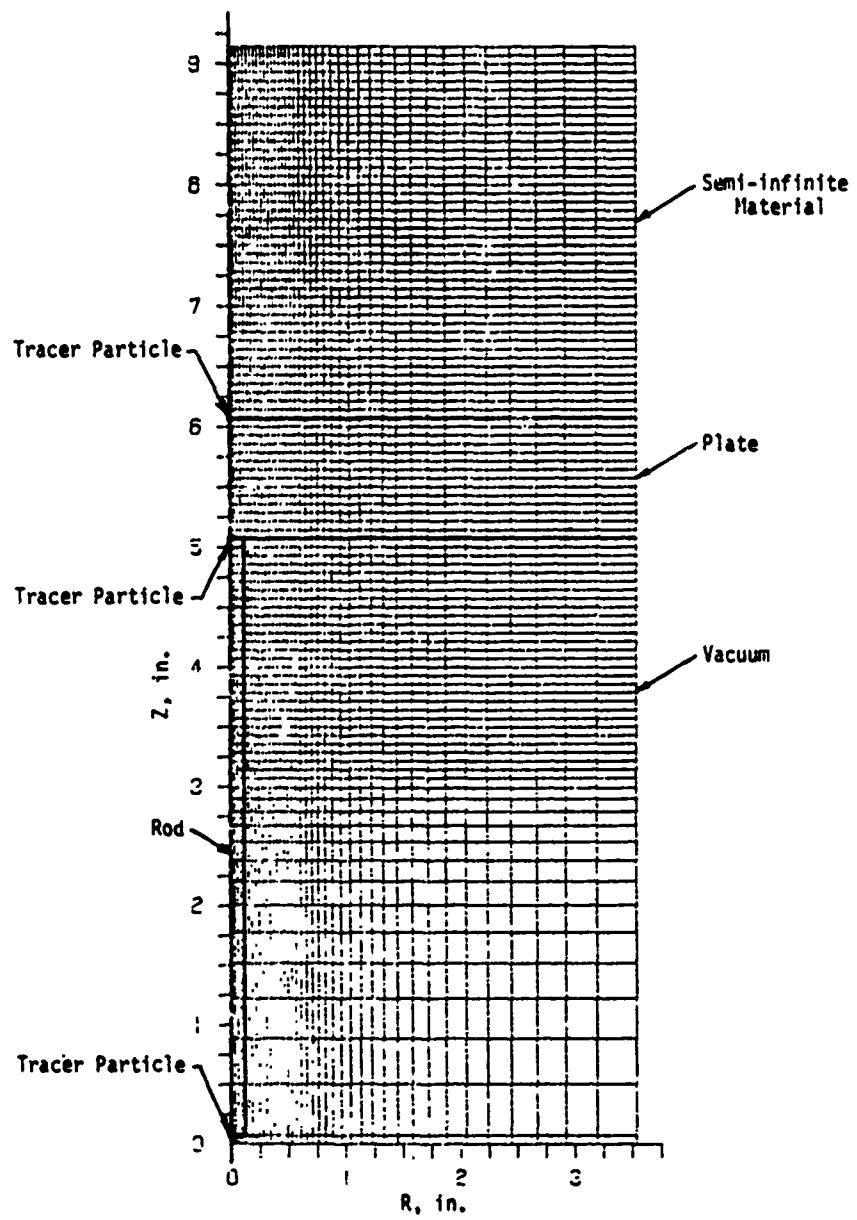
Figure 9 (U). Computational grid with an outline of
the projectile-target configuration and
the locations of the tracer particles.

35
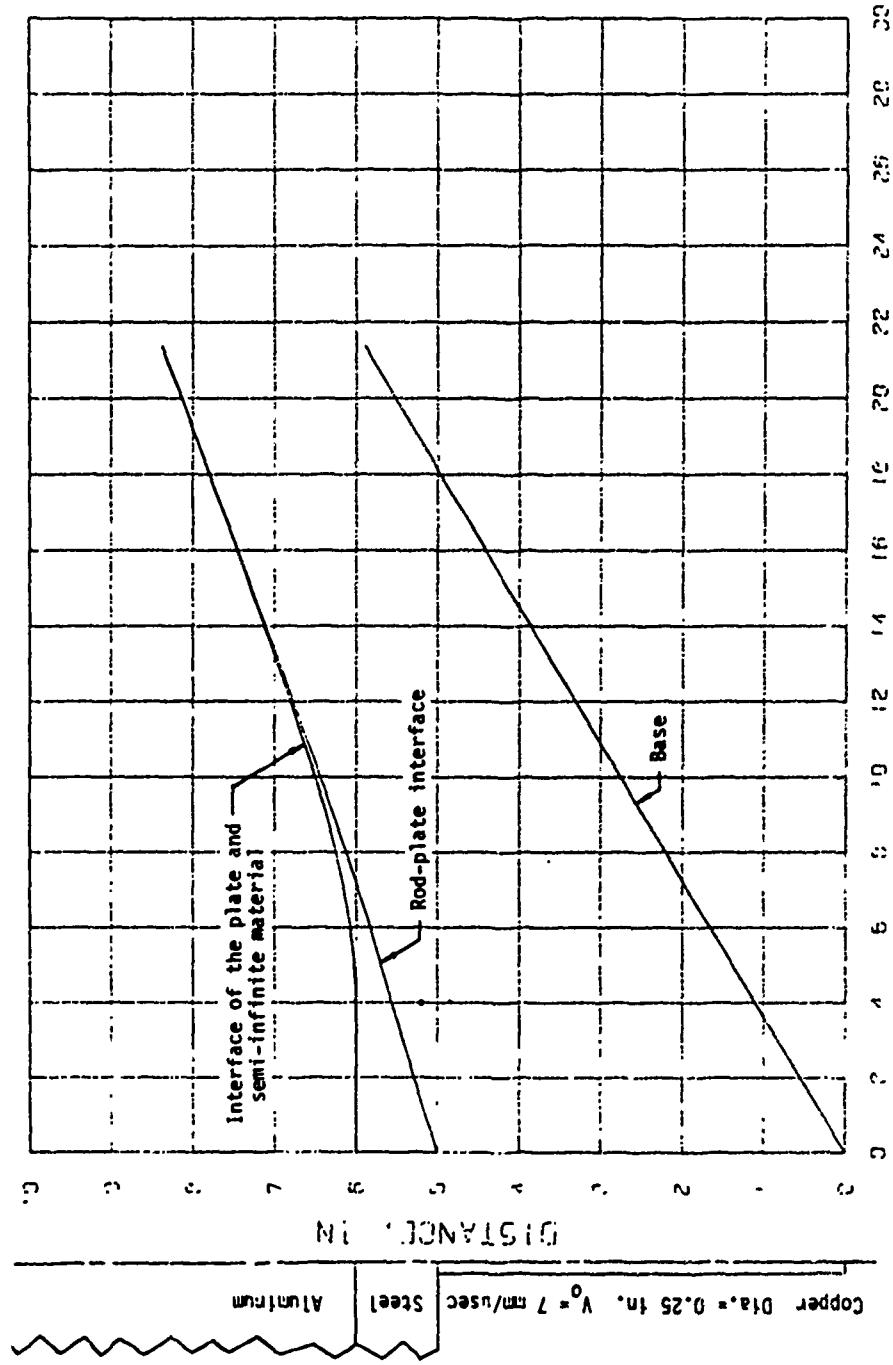
Figure 10 (U). The motion, along the axis of symmetry of a rod-target configuration, of three tracer particles is shown for Case 3.
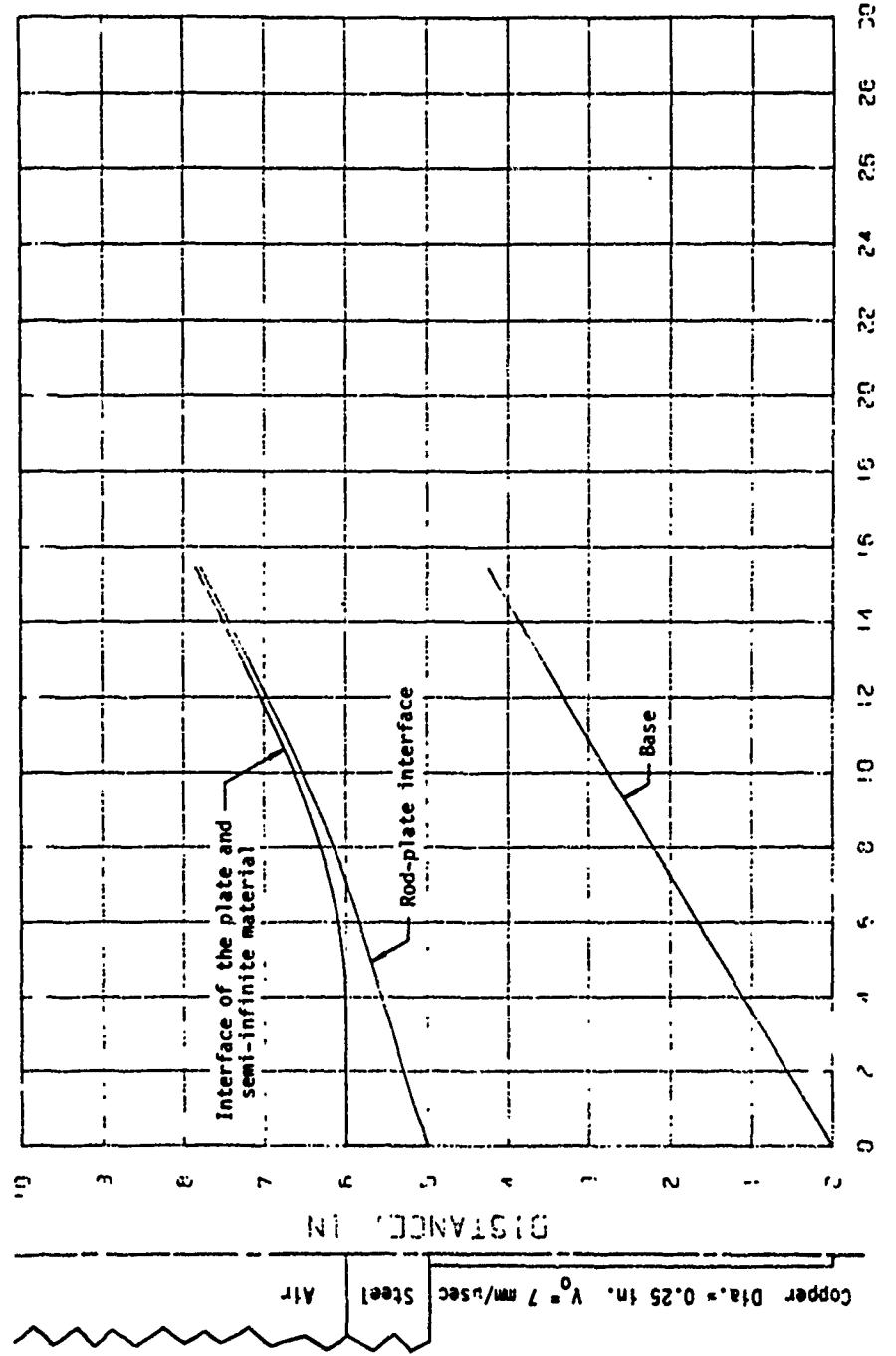
Figure 11 (U). The motion, along the axis of symmetry of a rod-target configuration, of three tracer particles is shown for Case 5.

37

TIME. MICROSEC
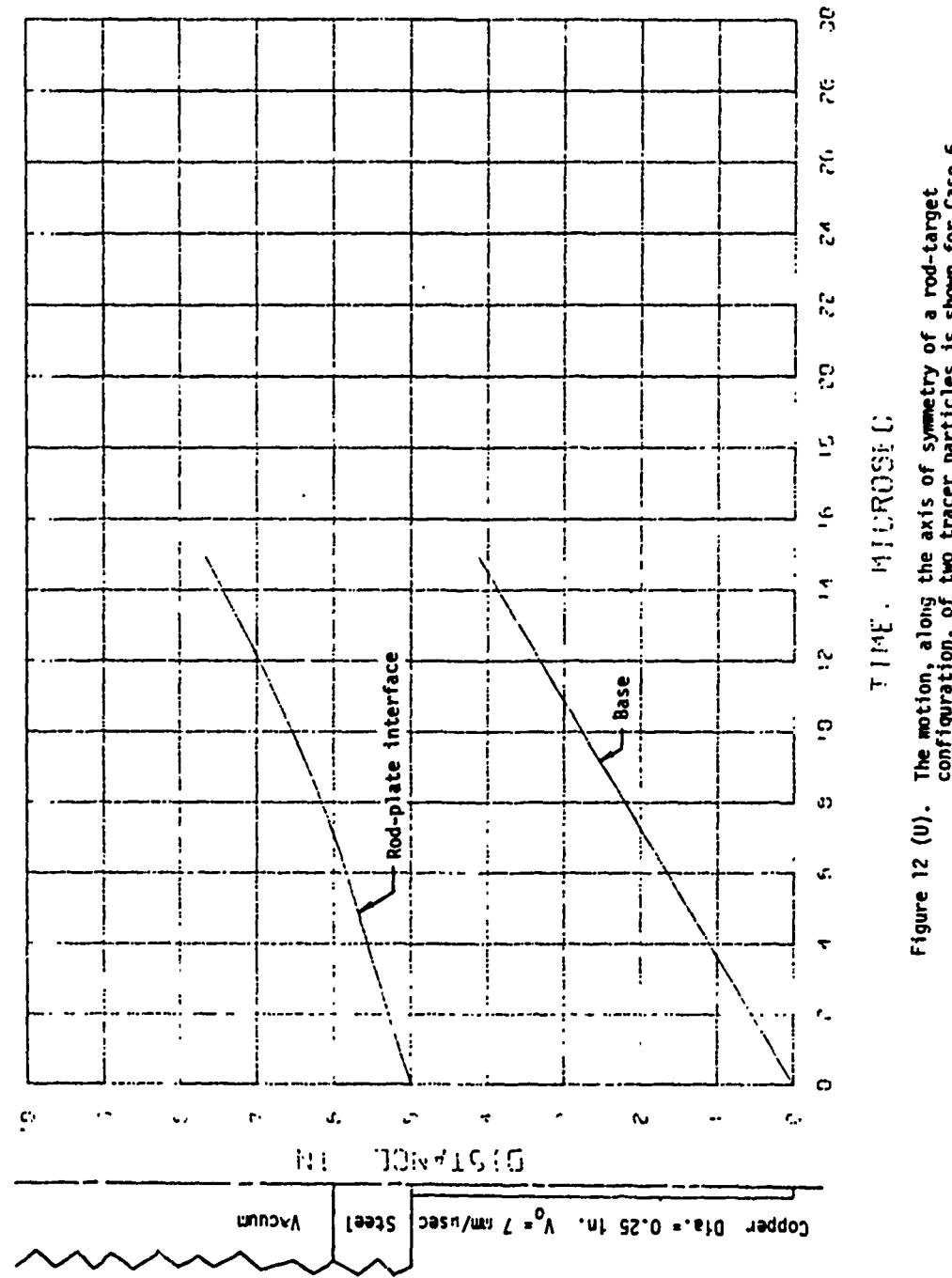
Figure 12 (U). The motion, along the axis of symmetry of a rod-target configuration, of two tracer particles is shown for Case 6.

38

TIME, MICROSEC
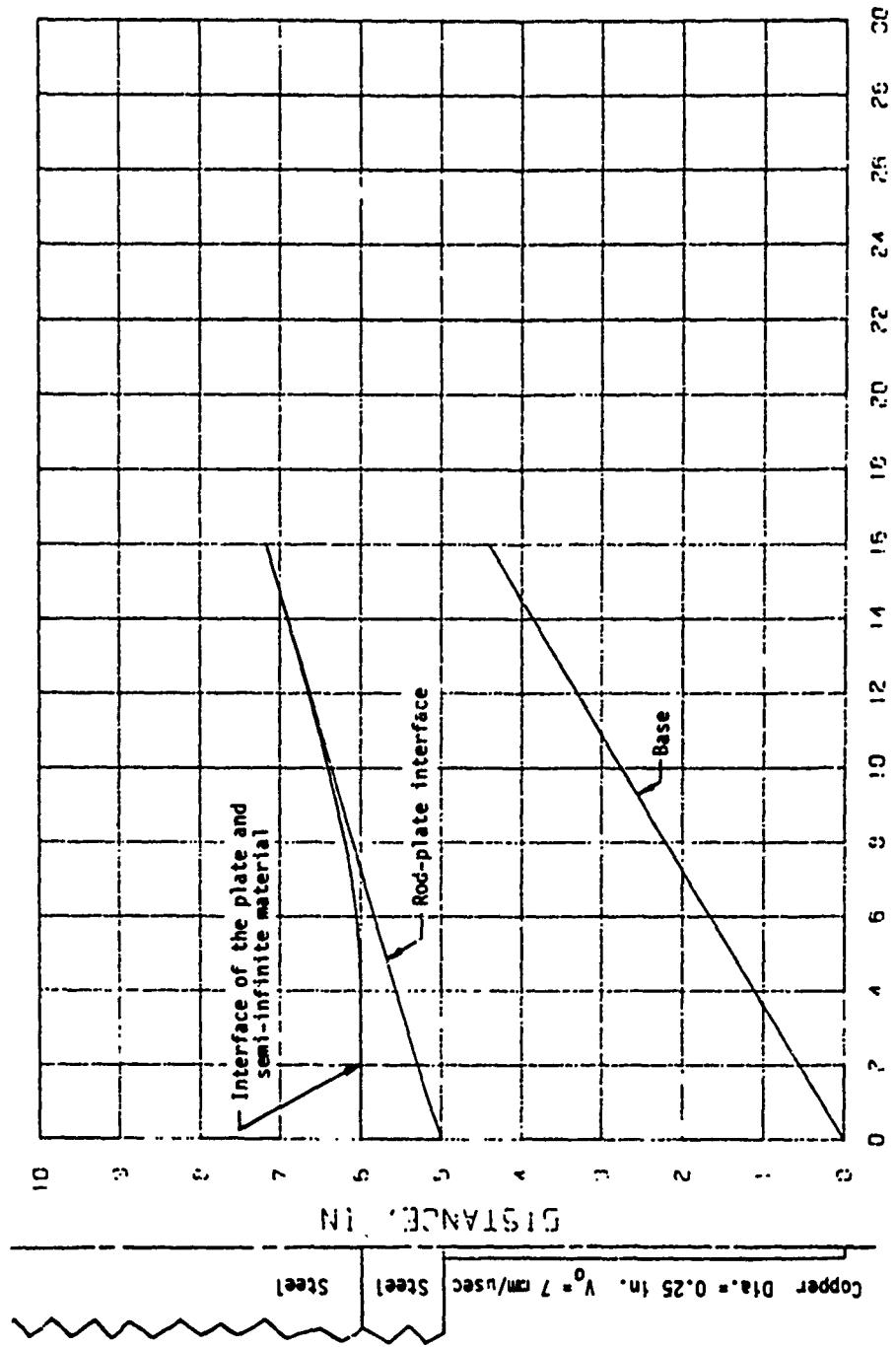
Figure 13 (U). The motion, along the axis of symmetry of a rod-target configuration, of three tracer particles is shown for Case 7.

39

TIME, MICROSEC
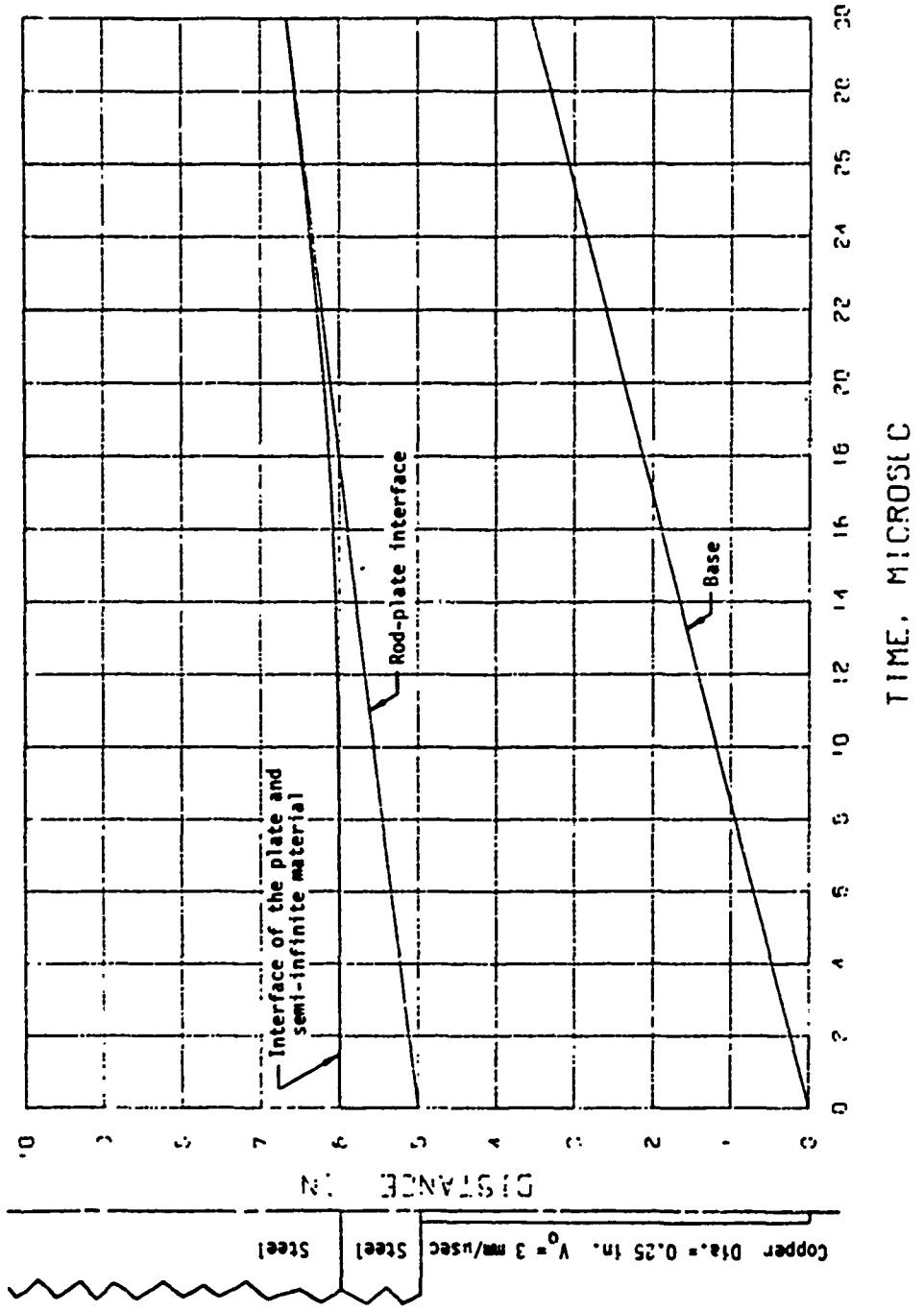
Figure 14 (U). The motion, along the axis of symmetry of a rod-target configuration, of three tracer particles is shown for Case 9.

TIME, MICROSEC
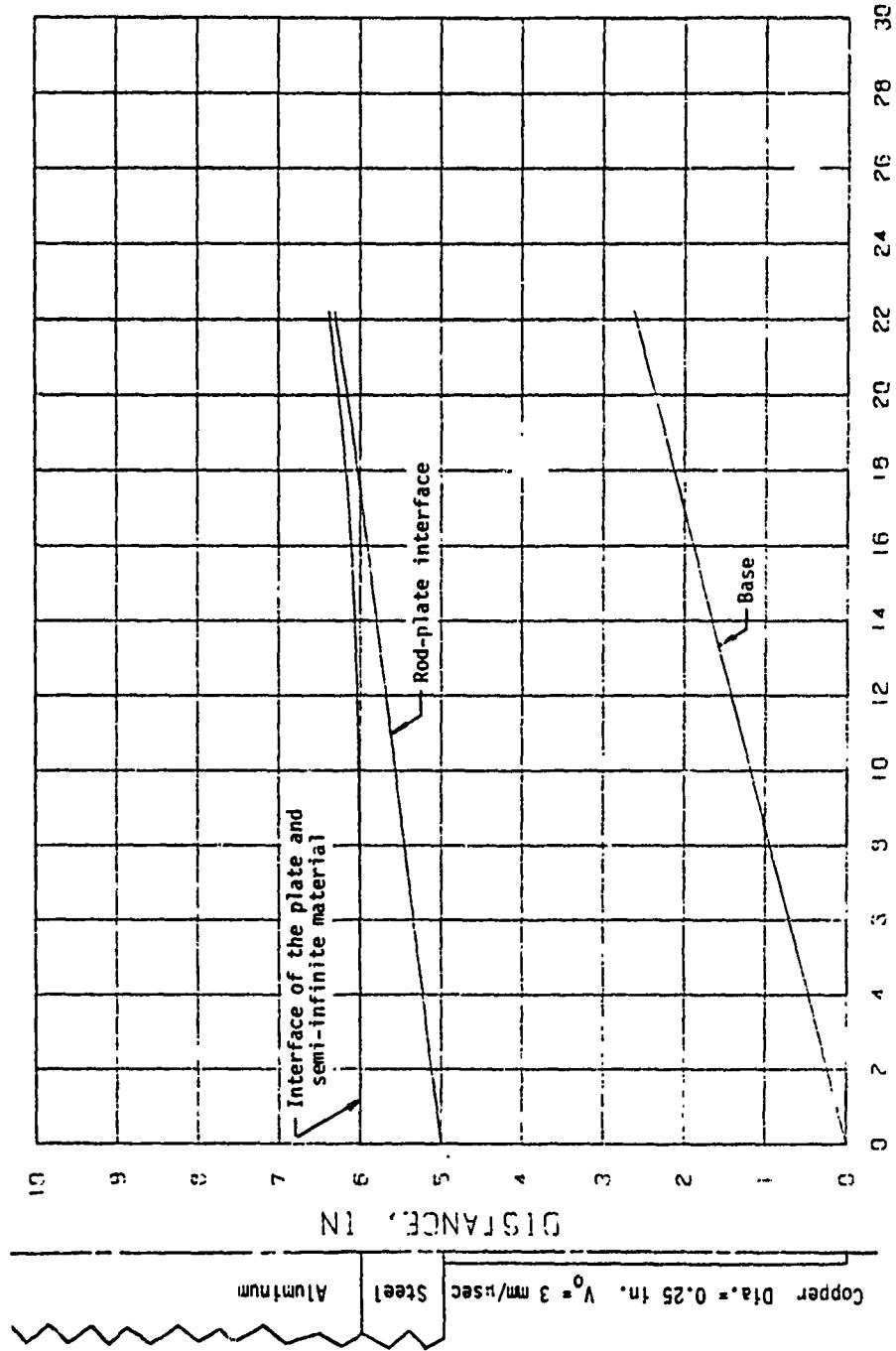
Figure 15 (U). The motion, along the axis of symmetry of a rod-target configuration, of three tracer particles is shown for Case 11.

41
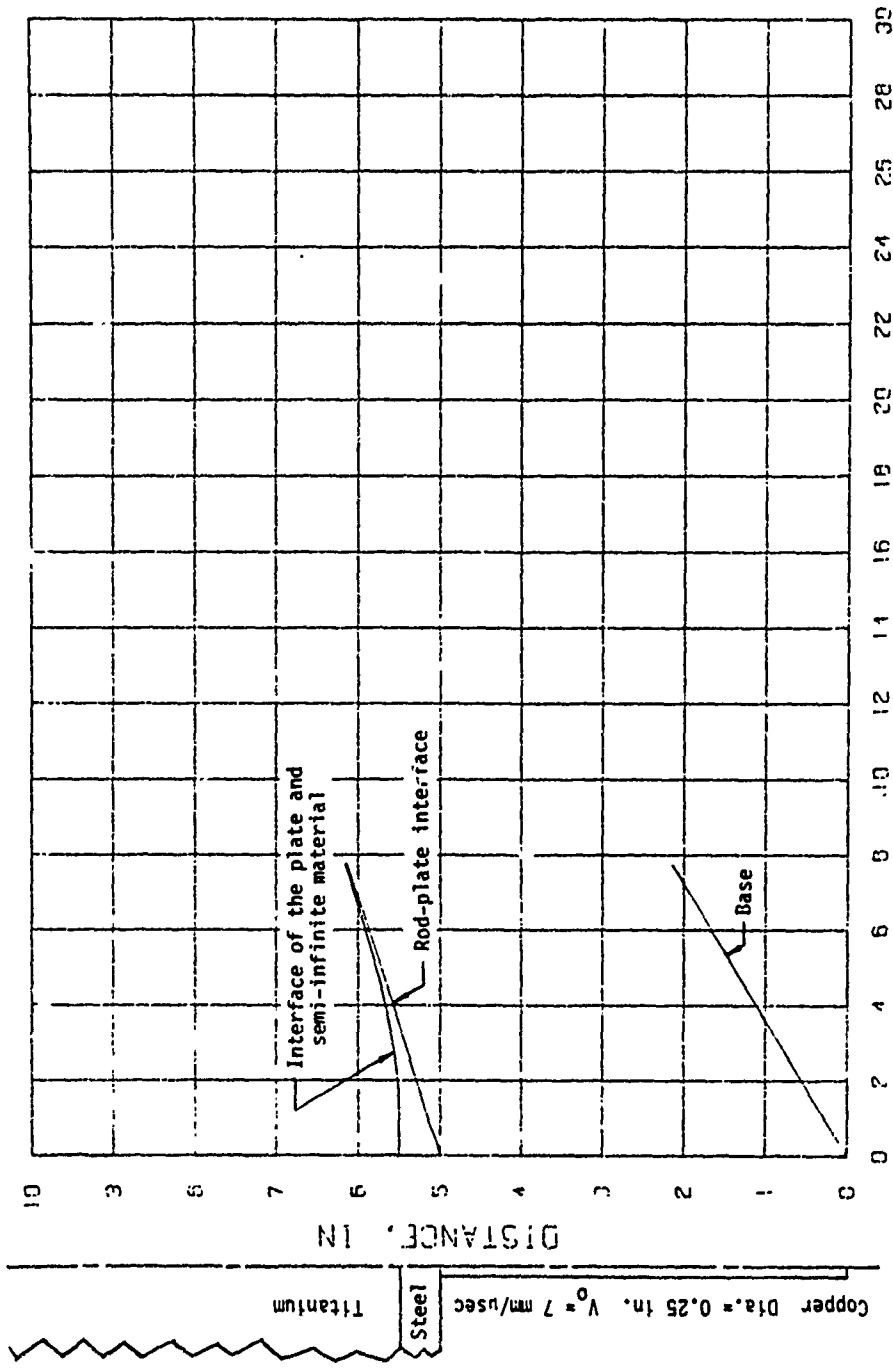
Figure 16 (U). The motion, along the axis of symmetry of a rod-target configuration, of three tracer particles is shown for Case 12.
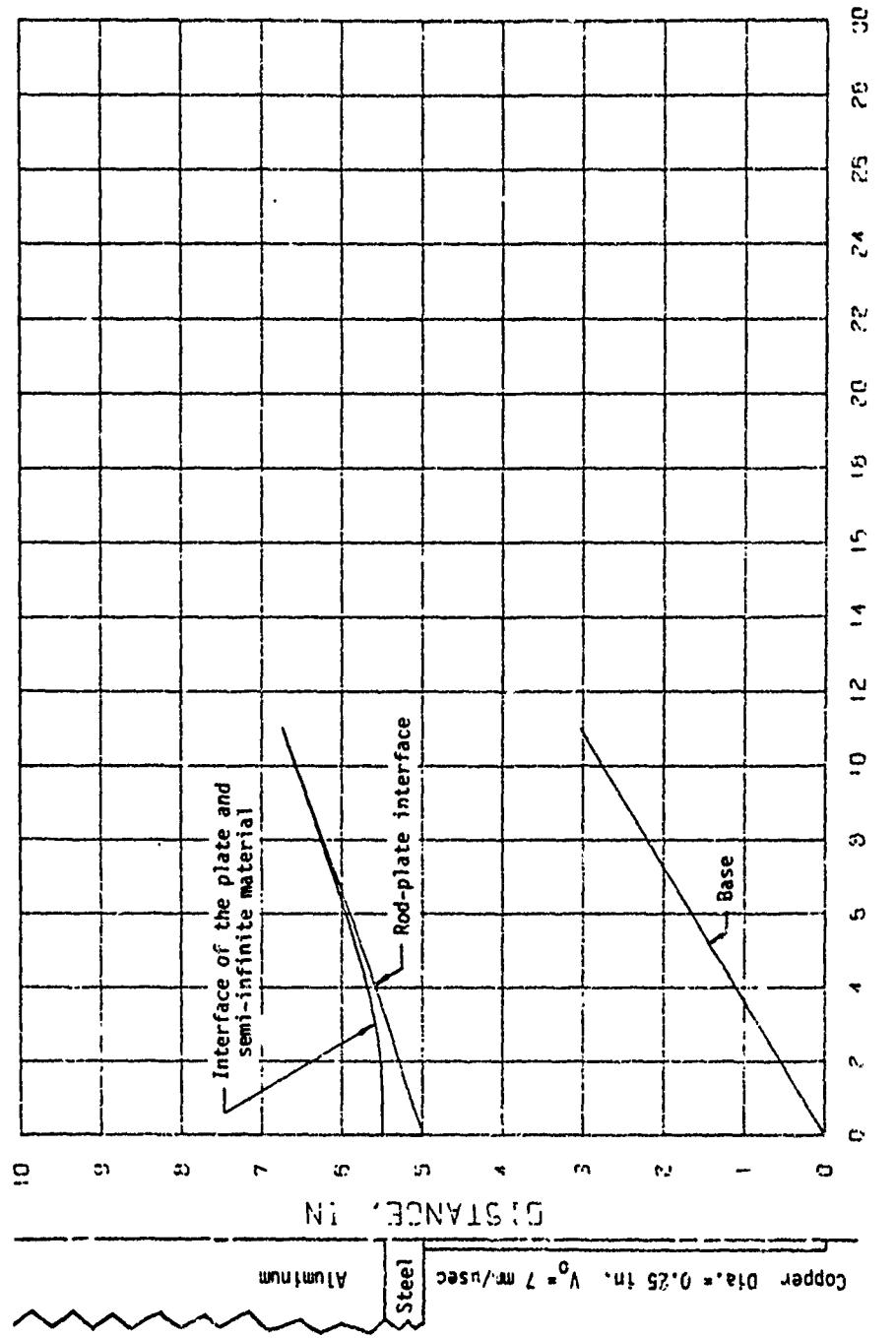
Figure 17 (II). The motion, along the axis of symmetry of a rod-target configuration, of three tracer particles is shown for Case 13.

43
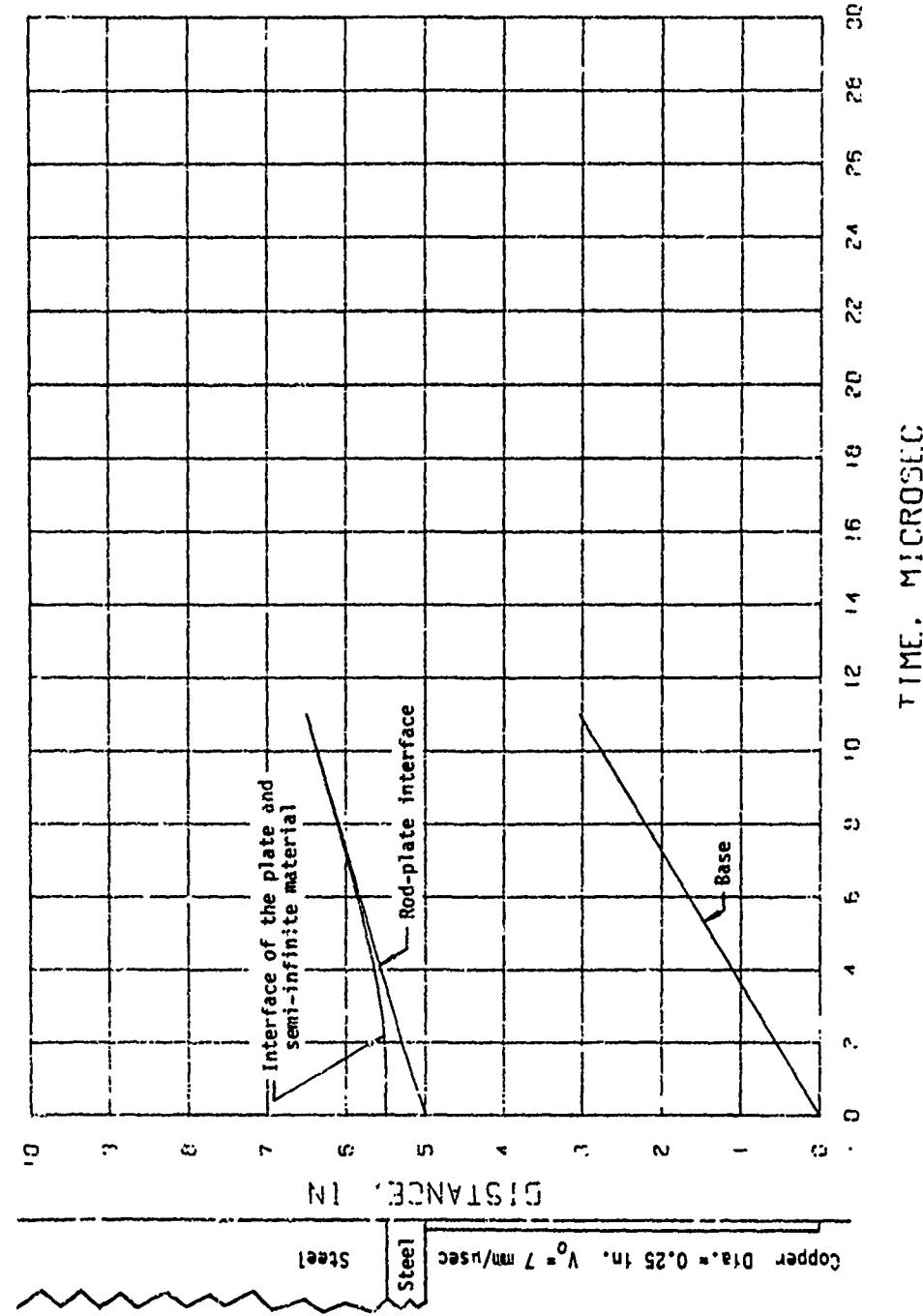
Figure 18 (U). The motion, along the axis of symmetry of a rod-target configuration, of three tracer particles is shown for Case 14.
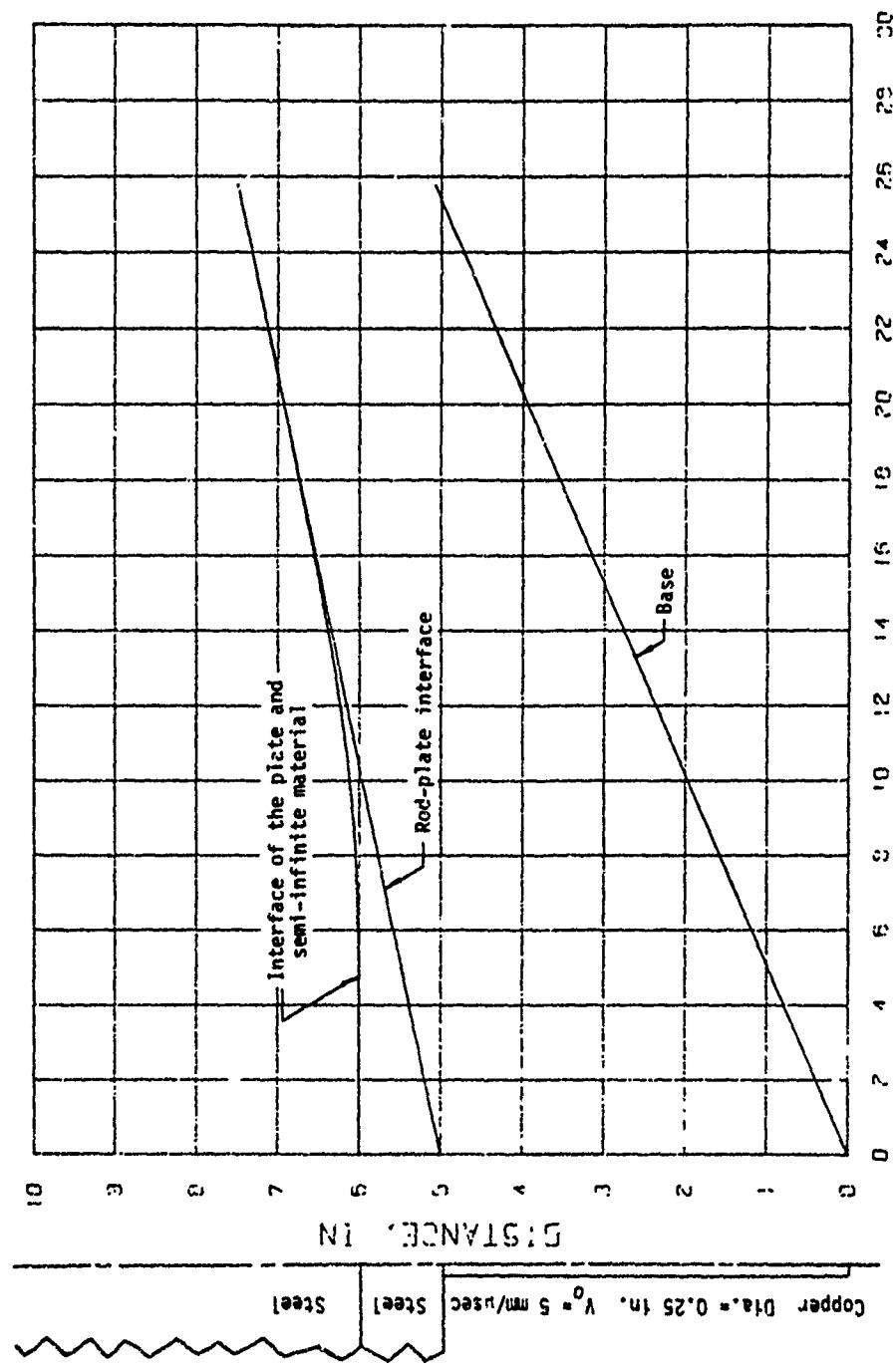
44

TIME, MICROSEC

Figure 19 (U). The motion, along the axis of symmetry of a rod-target configuration, of three tracer particles is shown for Case 15.

45
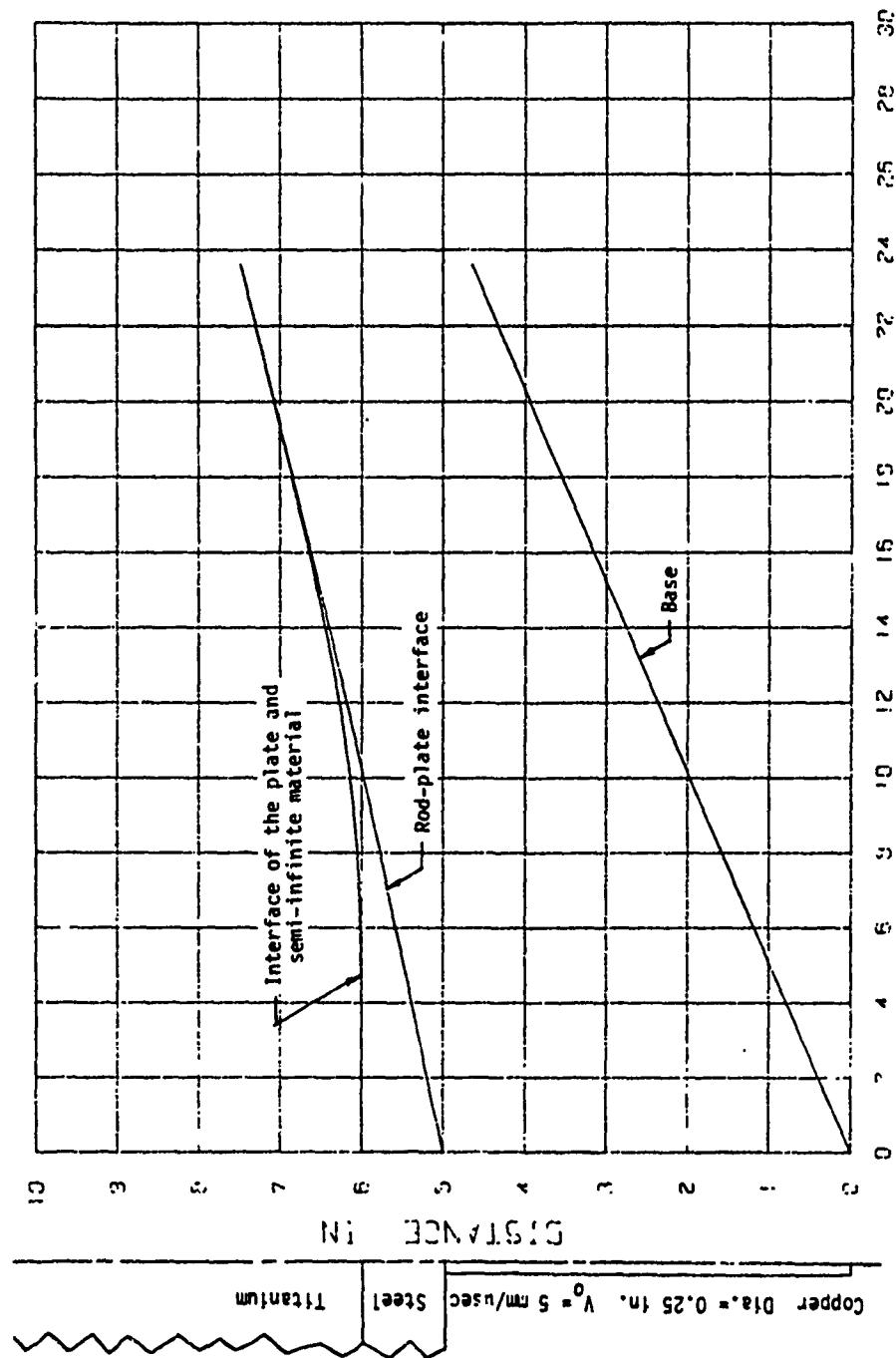
Figure 20 (U). The motion, along the axis of symmetry of a rod-target configuration, of three tracer particles is shown for Case 16.

46
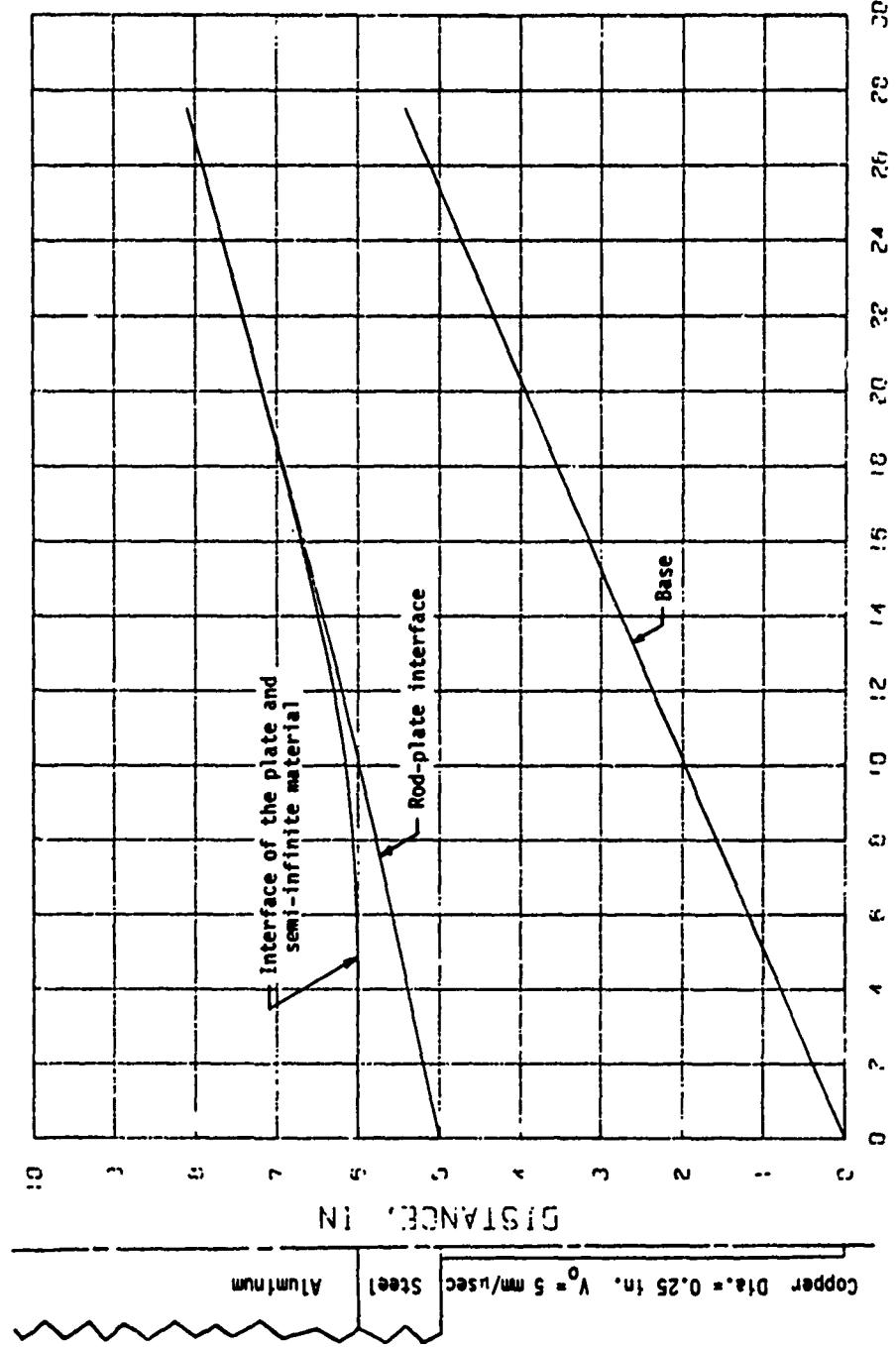
Figure 21 (U). The motion, along the axis of symmetry of a rod-target configuration, of three tracer particles is shown for Case 17.

47
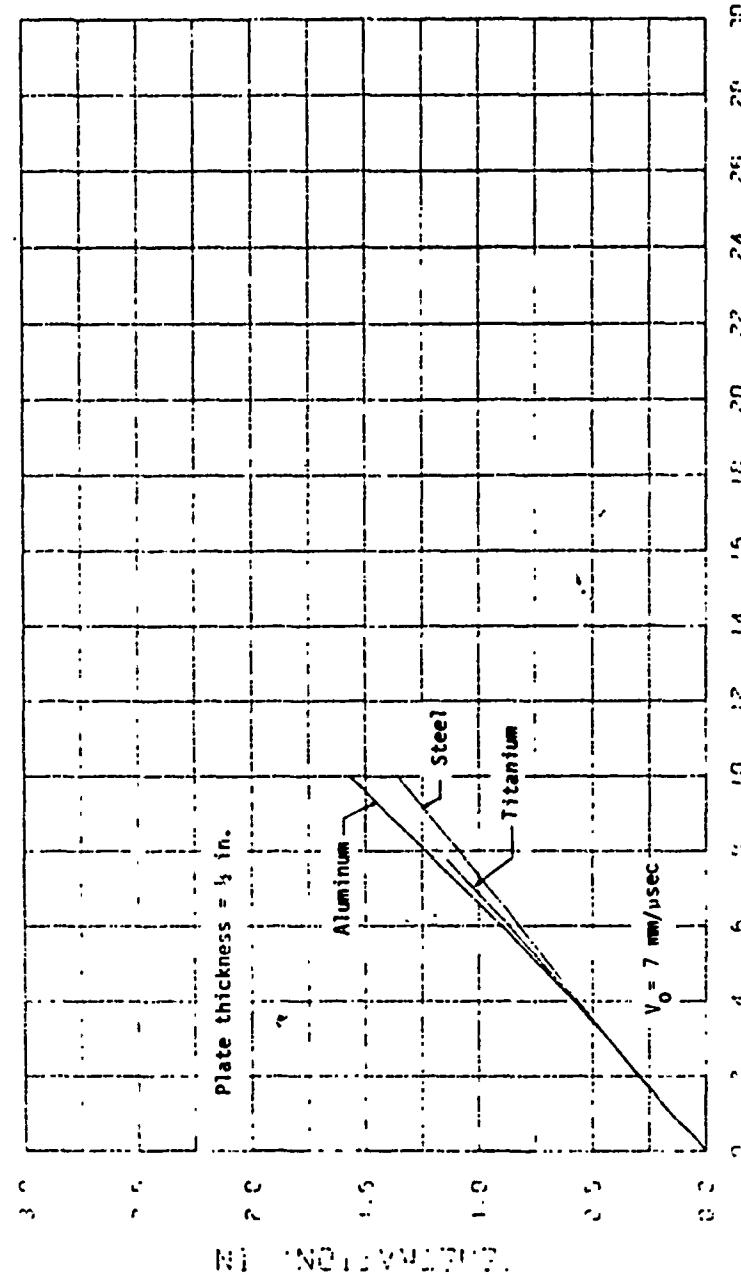
Figure 22 (U). The effect of density on the penetration history of a copper rod, impacting at $V_0 = 7$ mm/µsec on a ½-in. steel plate, which is backed by various materials, is shown.

48
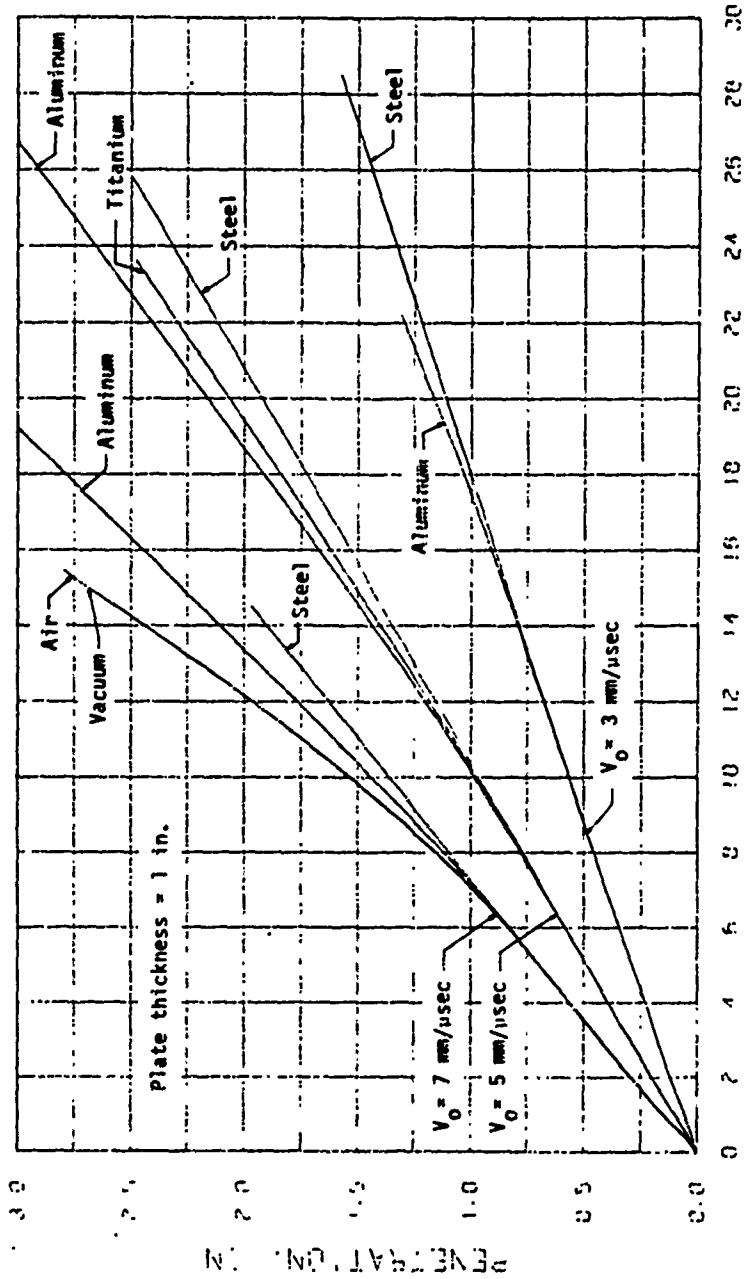
Figure 23 (U). The effects of density and initial impact velocity on the penetration history of a copper rod, impacting on a 1-in. steel plate, which is backed by various materials, are shown.

49

TIME, MICROSEC
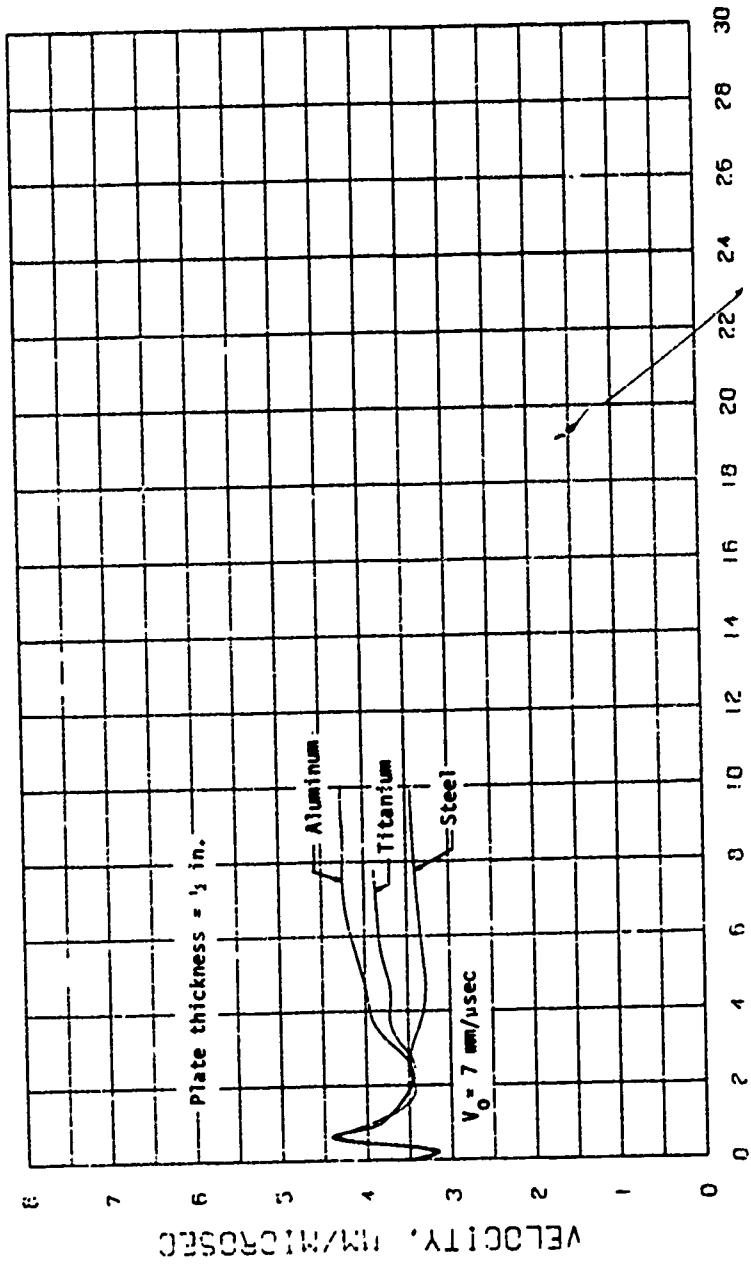
Figure 24 (U).   The effect of density on the penetration velocity history of a copper rod, impacting at V_0 = 7 mm/μsec on a ½-in. steel plate, which is backed by various materials, is shown.

50
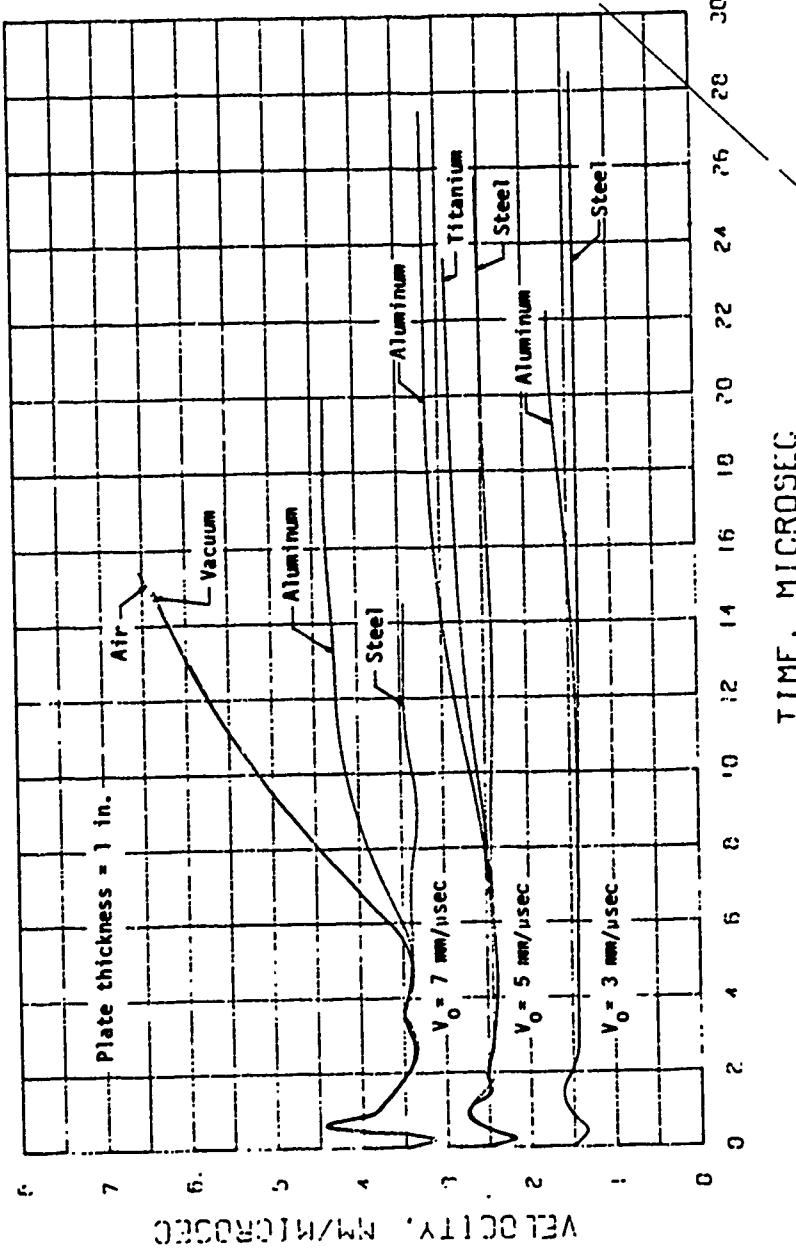
Figure 25 (U). The effects of density and initial impact velocity on the penetration velocity history of a copper rod, impacting on a 1-in. steel plate, which is backed by various materials, are shown.
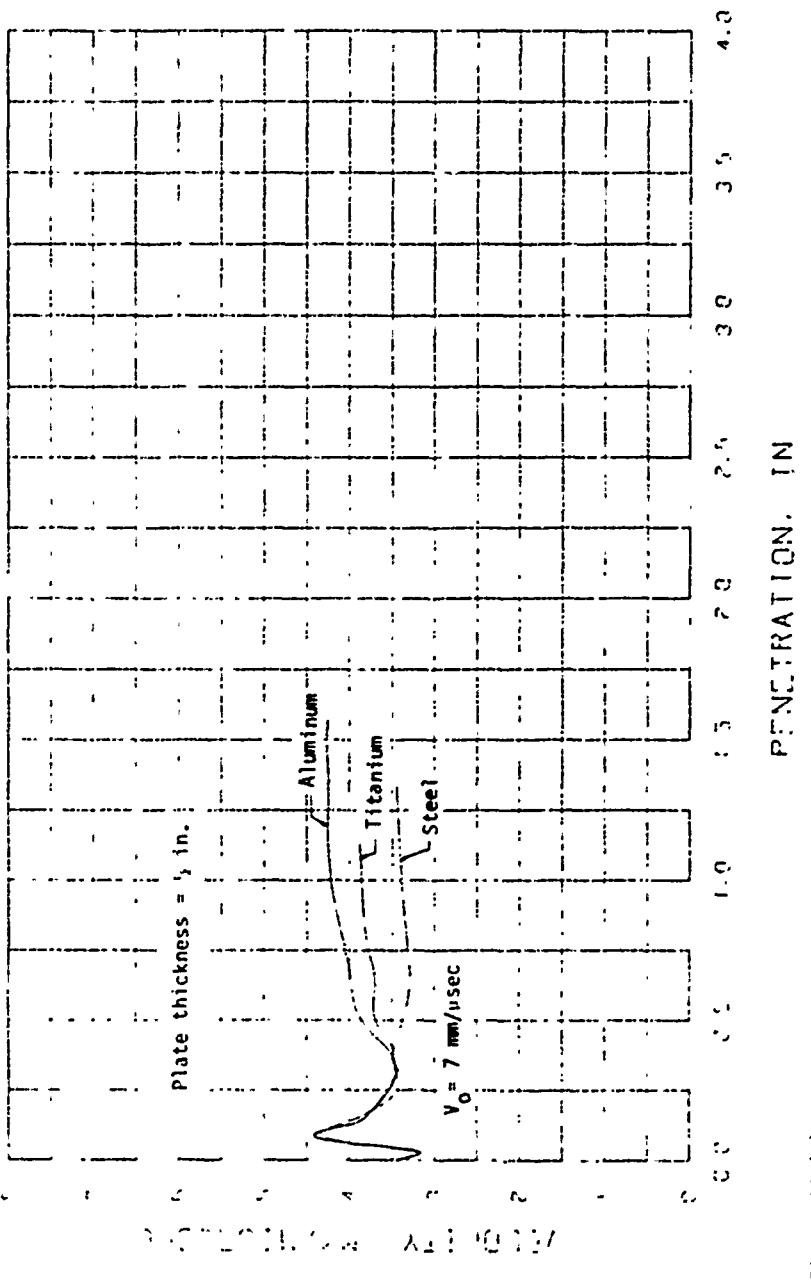
Figure 26 (U). The effect of density on the penetration velocity - penetration relationship for a copper rod, impacting at $V_o = 7$ mm/μsec on a ½-in. steel plate, which is backed by various materials, is shown.
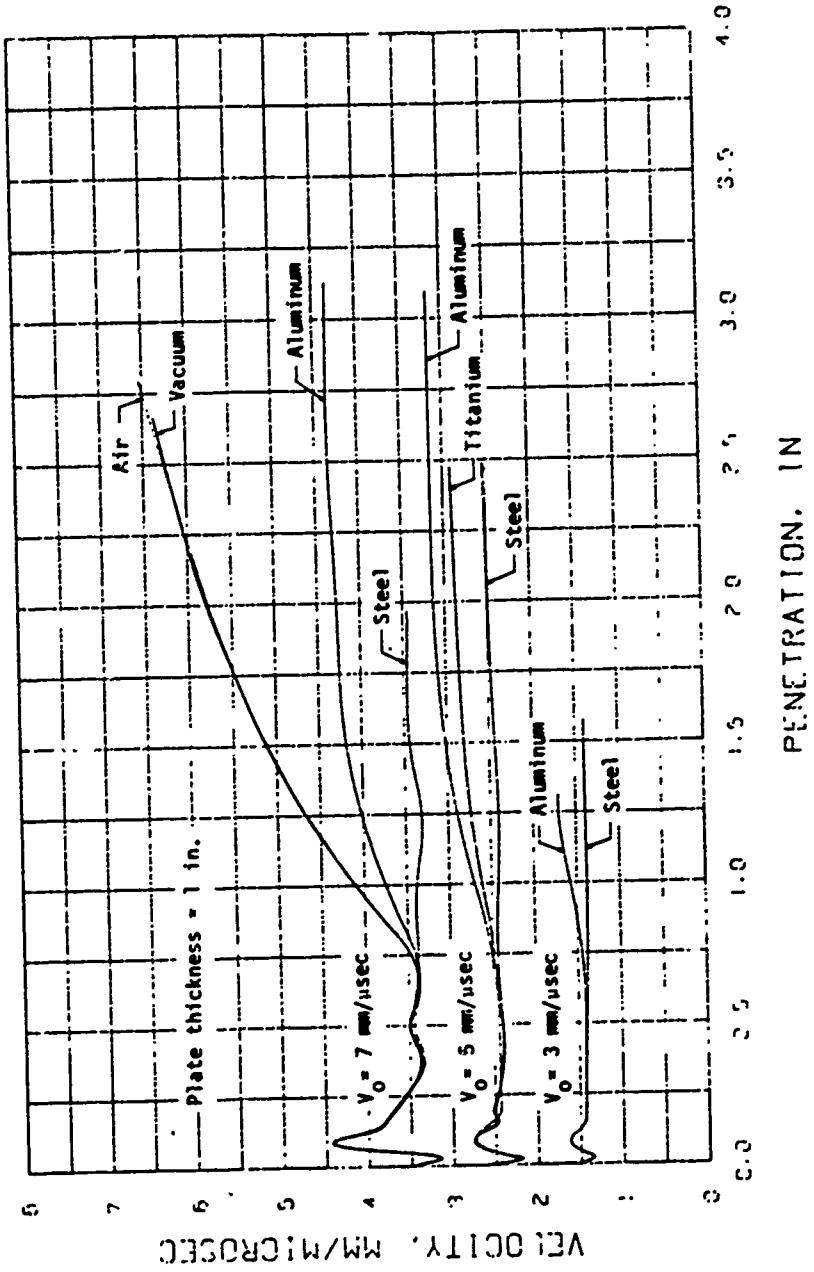
Figure 27 (U). The effects of density and initial impact velocity on the penetration velocity - penetration relationship for a copper rod, impacting on a 1-in. steel plate, which is backed by various materials, are shown.

53
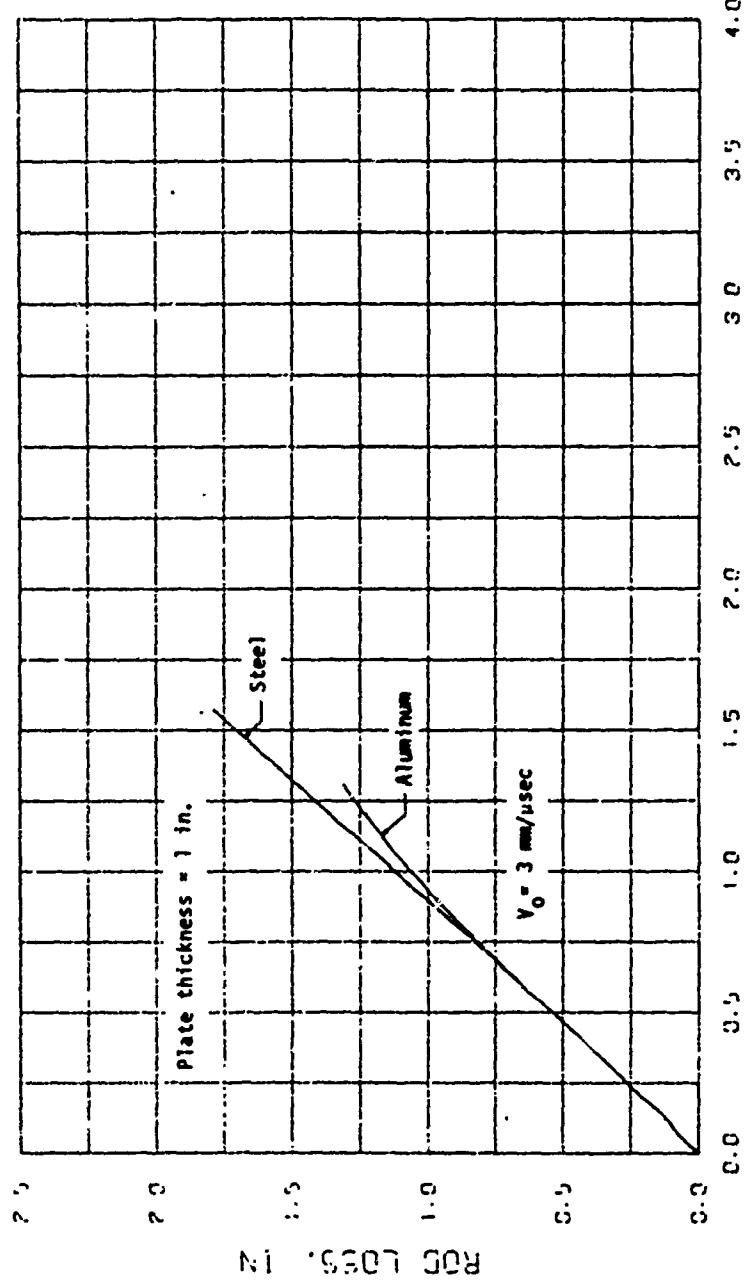
FENETRATION. IN

Figure 28 (U). The effect of density on the rod loss - penetration relationship for a copper rod, impacting at V_o = 3 mm/usec on a 1-in. steel plate, which is backed by various materials, is shown.

Plate thickness = 1 in.

Steel

Aluminum

V_o = 3 mm/usec

ROD LOSS, IN

54

PENETRATION. IN

Figure 29 (U). The effect of density on the rod loss - penetration relationship for a copper rod, impacting at $V_0 = 5$ mm/usec on a 1-in. steel plate, which is backed by various materials, is shown.

55
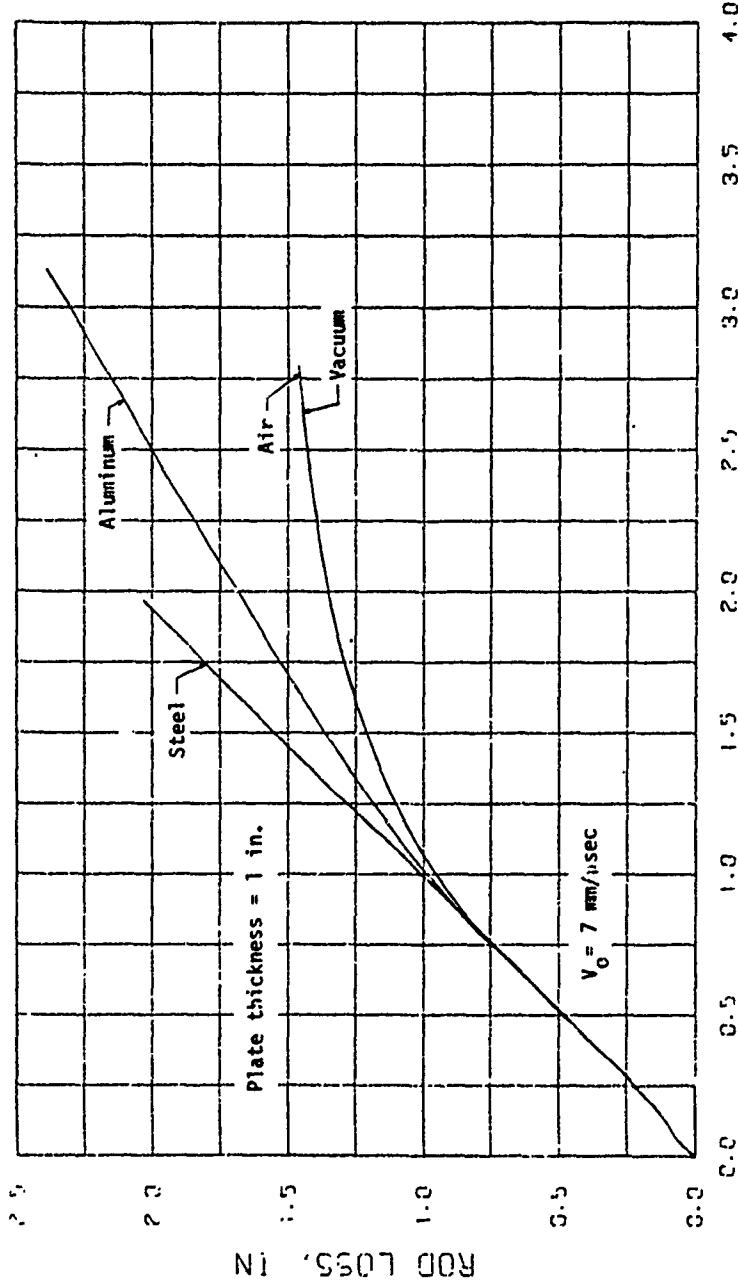
Figure 30 (U). The effect of density on the rod loss – penetration relationship for a copper rod, impacting at V_0 = 7 mm/usec on a 1-in. steel plate, which is backed by various materials, is shown.

56

PENETRATION. IN

Figure 31 (U). The effect of density on the rod loss - penetration relationship for a copper rod, impacting at V_0 = 7 mm/usec on a ½-in. steel plate, which is backed by various materials, is shown.

57
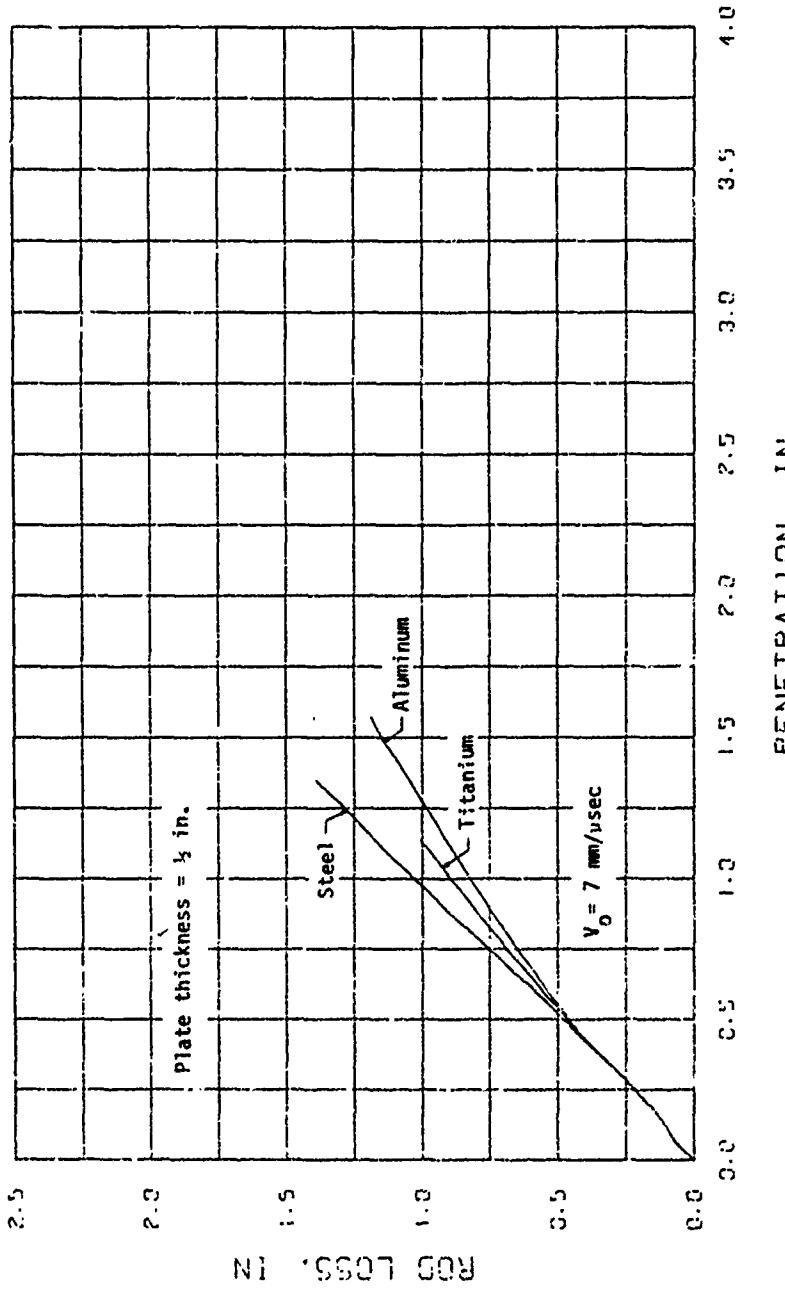
Figure 32 (U). The ratio of the apparent density of the target material to the ambient density of the target material is shown for the penetration of a copper rod, impacting at V_0 = 3 mm/usec on a 1-in. steel plate, which is backed by various materials.

58
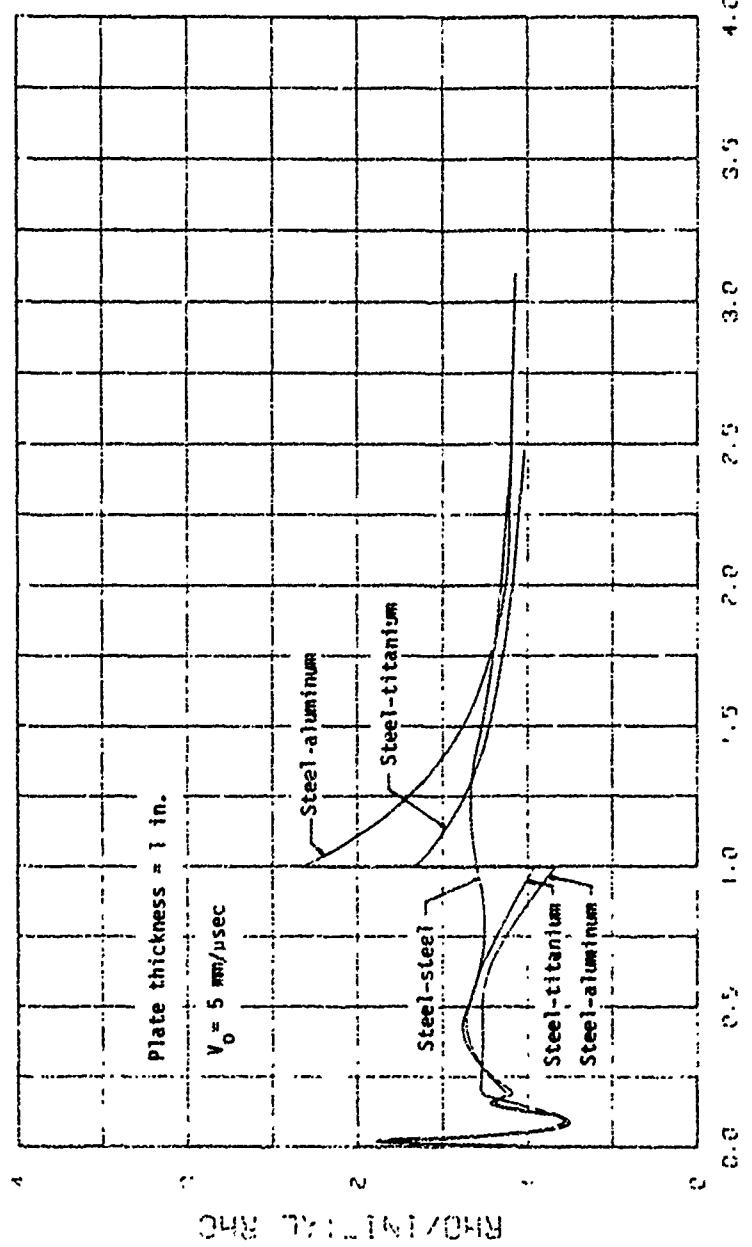
PENETRATION, IN

Figure 33 (U). The ratio of the apparent density of the target material to the ambient density of the target material is shown for the penetration of a copper rod, impacting at $V_o = 5$ mm/μsec on a 1-in. steel plate, which is backed by various materials.

59
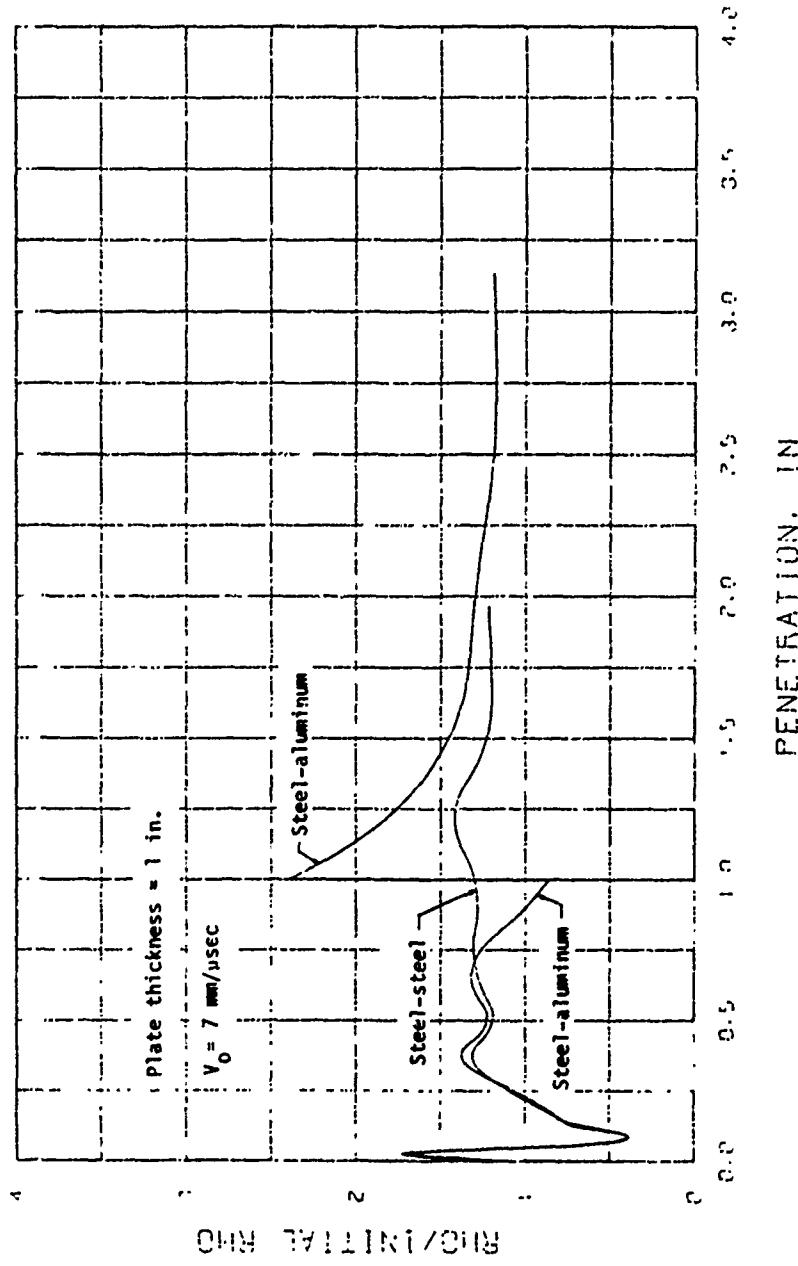
Figure 34 (U). The ratio of the apparent density of the target material to the ambient density of the target material is shown for the penetration of a copper rod, impacting at V_o = 7 mm/μsec on a 1-in. steel plate, which is backed by various materials.
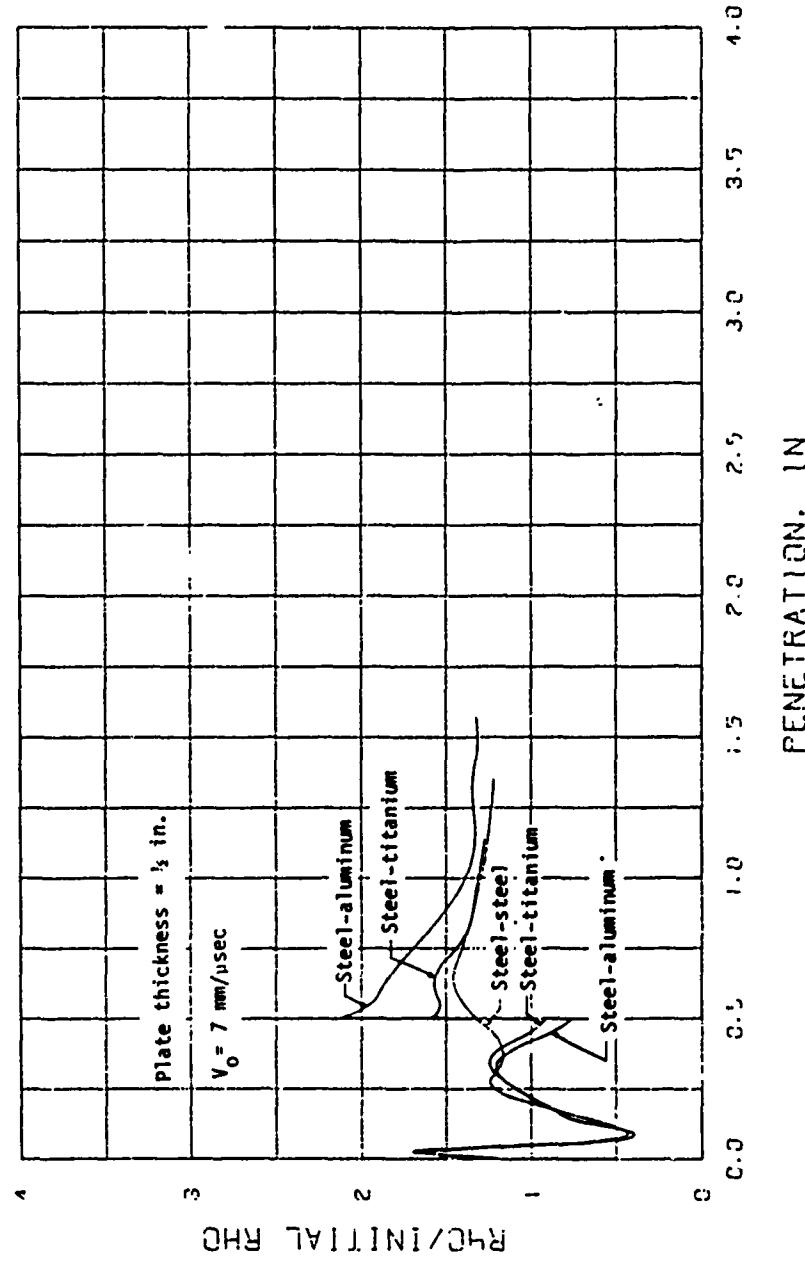
PENETRATION, IN

Figure 35 (U). The ratio of the apparent density of the target material to the ambient density of the target material is shown for the penetration of a copper rod, impacting at $V_0 = 7$ mm/μsec on a ½-in. steel plate, which is backed by various materials.

DISTRIBUTION LIST

No. of Copies	Organization	No. of Copies	Organization
12	Commander Defense Documentation Center ATTN: DDC-TCA Cameron Station Alexandria, VA 22314	2	Commander US Army Mobility Equipment Research & Development Command ATTN: Tech Docu Cen, Bldg. 315 DRDME-RZT Fort Belvoir, VA 22060
1	Commander US Army Materiel Development and Readiness Command ATTN: DRCDMA-ST 5001 Eisenhower Avenue Alexandria, VA 22333	1	Commander US Army Armament Materiel Readiness Command Rock Island, IL 61202
1	Commander US Army Aviation Systems Command ATTN: DRSAV-E 12th And Spruce Streets St. Louis, MO 63166	2	Commander US Army Armament Research and Development Command ATTN: Mr. J. Pearson Tech Lib Dover, NJ 07801
1	Director US Army Air Mobility Research and Development Laboratory Ames Research Center Moffett Field, CA 94035	1	Commander US Army Harry Diamond Labs ATTN: DRXDO-TI 2800 Powder Mill Road Adelphi, MD 20783
1	Commander US Army Electronics Command ATTN: DRSEL-RD Fort Monmouth, NJ 07703	1	Commander US Army Materials and Mechanics Research Center ATTN: Tech Lib Watertown, MA 02172
1	Commander US Army Missile Research and Development Command ATTN: DRDMI-R Redstone Arsenal, AL 35809	1	Director US Army TRADOC Systems Analysis Activity ATTN: ATAA-SA White Sands Missile Range NM 88002
1	Commander US Army Tank Automotive Development Command ATTN: DRDTA-RWL Warren, MI 48090	1	Assistant Secretary of the Army (R&D) ATTN: Asst for Research Washington, DC 20310

DISTRIBUTION LIST

No. of Copies	Organization	No. of Copies	Organization

2	Chief of Naval Research
	Department of the Navy
	ATTN: Code 427
	     Code 470
	Washington, DC 20325
		1	US Air Force Academy
			ATTN: Code FJS-RL (NC)
			     Tech Lib
			Colorado Springs, CO 80940

2	Commander US Naval Air Systems Command ATTN: Code AIR-310 Code AIR-350 Washington, DC 20360	1	Commander ATTN: Code OOAMA (MMECB) Hill AFB, UT 84401
1	Commander US Naval Ordnance Systems Command ATTN: Code ORD-0332 Washington, DC 20360	1	AFWL (SUL) Kirtland AFB, NM 87116
1	Commander US Naval Surface Weapons Center ATTN: Tech Lib Dahlgreen, VA 22448	1	AFLC (MMWMC) Wright-Patterson AFB, OH 45433
1	Commander US Naval Surface Weapons Center ATTN: Code 730, Lib Silver Spring, MD 20910	1	AFAL (AVW) Wright-Patterson AFB, CH 45433
1	Commander US Naval Weapons Center ATTN: Code 45, Tech Lib China Lake, CA 93555	1	Director National Aeronautics and Space Administration Langley Research Center Langley Station Hampton, VA 23365
1	Commander US Naval Research Laboratory Washington, DC 20375	1	Director Lawrence Radiation Laboratory ATTN: Mr. M. Wilkins P. O. Box 808 Livermore, CA 94550
1	USAF (AFRDDA) Washington, DC 20330	1	Computer Code Consultants ATTN: Mr. W. Johnson 527 Glencrest Drive Solana Beach, CA 92075
1	AFSC (SDW) Andrews AFB Washington, DC 20331	1	Physics International Corp ATTN: Mr. L. Berham 2700 Merced Street San Leandro, CA 94577
		1	Sandia Laboratories ATTN: Dr. L. Bertholf P. O. Box 5800 Albuquerque, NM 87115

DISTRIBUTION LIST

No. of
Copies   Organization

1   Systems, Science and Software
    ATTN: Dr. R. Sedgwick
    P. O. Box 1620
    La Jolla, CA 92037

1   Drexel Institute of Technology
    Wave Propagation Research Center
    ATTN: Prof. P. Chou
    32nd & Chestnnut Streets
    Philadelphia, PA 19104

2   University of California
    Los Alamos Scientific Lab
    ATTN: Dr. J. M. Walsh
           Tech Lib
    P. O. Box 1663
    Los Alamos, NM 87545

Aberdeen Proving Ground

    Marine Corps Ln Ofc
    Dir, USAMSAA